Are there clouds on Ultra Hot Jupiters?

Alexandre Gillet, University of Potsdam, Golm, Germany, Leibniz-Institut fur Astrophysik (AIP), Babelsberg, Germany

May 2021

Contents

1 Acknowledgement

I would like to express my gratitude to my primary supervisor, Prof. Dr. Katja Poppenhäger, who guided me throughout this project during a worldwide pandemic. I would also like to thank my team from my institute, Leibniz-Institut fur Astrophysik (AIP), who offered precious help and deep insight into the study. I would like to thank my friends and family who supported me during this eventful year.

2 Abstract(DE)

Mit Entdeckung des ersten Exoplaneten im Jahr 1995, wurde eine neue Ära der Astrophysik eingeleitet. Bisher sind 4324 Exoplaneten entdeckt und bestätigt – Tausende werden folgen. Der Start der Weltraummission Kepler im Jahr 2009 markierte einen Wendepunkt in ihrer Entdeckung. Das Teleskop verhalf während seiner neunjährigen Umlaufbahn zur Entdeckung von mehr als 2600 Exoplaneten. Seitdem ist die Kategorisierung von Exoplaneten zwingend und wesentlich geworden. Mehrere effiziente Nachweismethoden zur Erkennung von Exoplaneten wurden entwickelt. Die Radialgeschwindigkeit und Transitmethode sind die beiden wichtigsten Detektionsmethoden, die heutzutage verwendet werden. Während die Radialgeschwindigkeit Informationen über die Masse des Planeten liefert, gibt die Transitmethode ihre Radien an. In Kombination geben beide Methoden eine ungefähre Auskunft über die Dichte und die Bestandteile eines Planeten.

Im Jahr 2001 beobachtete die Wissenschaftsgemeinde die erste Exoplanetare Atmosphäre Charbonneau et al. (2002), gefolgt vom ersten Nachweis einer atmosphärischen Emission einige Jahre später Charbonneau et al. (2005). Diese Entdeckungen ebneten den Weg für einen neuen, vielversprechenden und aufregenden Zweig der Astrophysik: Die Exometeorologie. Obwohl die individuelle Identifikation eines Exoplaneten zur relativen Routine geworden ist, ist es weitaus schwieriger dessen Planetenatmosphäre zu erkennen. Die Atmosphäre eines Exoplaneten kann unter anderem mithilfe der Transitmethode untersucht werden.

Die erste Technik, die als primärer Transit bezeichnet wird (der Planet passiert die Vorderseite des Sterns), dient zur Bestimmung der Temperaturstruktur und der chemischen Zusammensetzung der Atmosphäre über Transmissionsspektren. Eine zweite Technik, die als Sekundärtransit bezeichnet wird (wenn der Planet hinter dem Wirtsstern verschwindet), kann verwendet werden, um die Temperaturstruktur und die Albedo zu bestimmen. Diese Werte geben Auskunft über die Wolkendecke. Außerdem ist die Phasenkurve, die die Änderung der Helligkeit des Planeten als Funktion des Phasenwinkels beschreibt, ein leistungsfähiges Werkzeug, um die thermische Struktur, den Temperaturgradienten oder die Transportprozesse.

Diese Arbeit konzentriert sich hauptsächlich auf die zweite Technik: die Sekundärtransit. Die effizientesten Ziele zur Charakterisierung von Atmosphären sind bisher die Ultra Hot Jupiters (UHJ). Es handelt sich um eine stetig wachsende Klasse von gezeitengesperrten, riesigen, gasförmigen Exoplaneten mit kurzer Umlaufzeit, kleiner Semi-Major-Achse und sehr hoher Gleichgewichtstemperatur (höher als 2000 K). Die Bestimmung einer Sekundärtransit kann sehr schwierig sein, da die Tiefe der Sekundärtransit viel flacher ist als die Durchgangstiefe.

Das Hauptziel dieser Arbeit ist es, die zeitliche Variabilität der Eclipse-Tiefe mehrerer UHJ zu testen. Es ist zu erwarten, dass die Änderung der Albedo auch auf eine Änderung der Wolkendecke hindeutet. Es bleibt jedoch unklar, ob sich unter extremen Bestrahlungsbedingungen Wolken bilden können, wobei neuere Untersuchungen darauf schließen lassen. Tatsächlich bilden sich auf der weniger bestrahlten Nachtseite Wolken, auf denen Moleküle bei niedrigeren Temperaturen kondensieren und über den Tag- / Nacht-Terminator zur stärker bestrahlten Tages seite gelangen können. In dieser Arbeit habe ich die Variabilität der Finsternistiefe von vier exoplanetaren Systemen untersucht: WASP-18b, WASP-121b, KELT-1b und KELT-9b über die TESS-Daten (Transiting Exoplanet Survey Satellite). Jede sekundäre Finsternistiefe wurde separat mit einem Mandel-Agol-Modell Mandel & Agol (2002) unter Verwendung eines Python-Skripts von C. Von Essen von Essen et al. (2018)

untersucht. Das Skript verwendet eine skalierte Version des Transitmodells, die alle Stern- und Orbitalparameter implementiert. Es ist zu beachten, dass die Sternaktivität einen signifikanten Einfluss auf die dargestellten Beobachtungen haben kann. Daher wurden weitere Untersuchungen durchgeführt, um den Einfluss von Sternflecken auf die Lichtkurve zu testen. Sternenflecken können eine scheinbare Veränderung der Sekundärtransittiefe verursachen, ohne dass dies eine Albedoveränderung bedeuten muss.

3 Abstract(EN)

The first detection of an exoplanet in 1995 allowed us to step into a new era in astrophysics. So far, 4324 confirmed exoplanets has been found and thousands more to be discovered in the following years. The launch of the Kepler space mission in 2009 marked a turning point in their detection. Indeed, throughout its 9 years in orbit, the telescope was responsible for the discovery of more than 2600 exoplanets. Thenceforth, the categorisation of exoplanets has become imperative and essential. Moreover, several detection methods started to emerge and some of them even became very efficient to detect exoplanets. The radial velocity and transit method are the two major detection methods used nowadays. While the radial velocity gives information about the mass of the planet, the transit method will give its radii. Combining both, one obtains a rough idea of the planet's density and what the planet is mostly made of.

In 2001, the community observed the first exoplanetary atmosphere Charbonneau et al. (2002) followed by the first detection of an atmospheric emission a few years later Charbonneau et al. (2005). Those detections paved the way for a new promising and exciting branch in astrophysics: exo-meteorology. If detecting an exoplanet became quite a routine in the past years, detecting a planetary atmosphere is far more challenging. The atmosphere of an exoplanet can be studied trough different techniques via the transit method.

The first technique called the primary transit (when the planet transits in front of the star) enables us to unveil the chemical composition of the atmosphere via the transmission spectra. A second technique named the secondary eclipse (when the planet disappears behind the host star) can be used to determined the temperature structure and the albedo which in return gives us information about the cloud coverage. At last, the phase curve (which describes the variation of brightness of the planet as a function of the phase angle) is a powerful tool to constrain the thermal structure, temperature gradient or transports processes.

This work has been mostly focused on the second technique: the secondary eclipse. The best targets to characterise atmospheres so far are the Ultra Hot Jupiters (UHJ). It is a rising class of tidally locked giant gaseous exoplanets with short orbital period, small semi-major axis and very high equilibrium temperature (higher than 2000K). The detection of a secondary eclipse can be very testing since the eclipse depth is much more shallowing than the transit depth. The main goal in this work is to test the time variability of the eclipse depth of several UHJ which suggests a change in the albedo and in return a change in the cloud coverage.

Nevertheless, it remains unclear if clouds can form under such extreme irradiated regime. However, recent investigations indicate that they can form, but under specific conditions. Indeed, clouds form on the unirradiated night side where molecules condense at lower temperatures and may travel to the irradiated day side via the day/night terminator. In this work, I have examined and studied the eclipse depth variability of four exoplanetary sys-

tems: WASP-18b, WASP-121b, KELT-1b and KELT-9b via the Transiting Exoplanet Survey Satellite (TESS) data.

Each eclipse was fit individually with a Mandel-Agol Model Mandel & Agol (2002), using a python script written by C. Von Essen von Essen et al. (2018). However, the script uses a scale version of the transit model which implements all the stellar and orbital parameters. Furthermore, the stellar activity may have a significant impact on the observations and further investigations have been made to test the influence of stellar spots on the light curve. The presence of stellar spots can trigger a real detection of the time variability of the transit or the secondary eclipse depth.

4 Introduction

The past decade and even more recent findings in the exoplanet field have exhibited colossal data and fantastic discoveries. From the first detection of an exoplanet around the pulsar PSR 1257+12 in 1992 to the first detection of a thermal emission from the extrasolar planet TrES-1 in 2005, a tremendous work of characterisation and classification of exoplanets has begun. Because our solar system contains an extraordinary variety of celestial objects, each as unique as the other, having an identical twin seems to be very unrealistic. Unlike their parent stars, planets exhibit a higher level of complexity. For instance, the physical and chemical processes in place within the protoplanetary disk at the moment of their birth are still poorly understood. In addition of being intricate objects, extrasolar planets are also very difficult to detect. Obviously, detecting an Earth-like planet located a few light years away require a very high spatial resolution space telescope. Luckily, substantial developments have been made in the past years that now allow us to detect them due to extensive photometry and high resolution spectroscopy. This unlocked some mysteries of planetary formation and evolution.

New fields have emerged more recently: extrasolar climatology and exo-meteorology. Indeed, the observation and the study of exoplanetary atmospheres have tremendously grown in the past decade. Space surveys such as SPITZER, KEPLER and TESS offered us an extremely large sample of data and a very wide variety of new worlds to explore. A good way to modelize and probe their atmosphere is to first look at much closer objects: planets and moons of our solar system. Indeed, our solar system represents the best laboratory so far in order to examine the myriad of physical processes responsible for such diversity.

For example : Mercury, Enceladus (Saturn's moon) and Titania (Uranus moon) are bodies with an extremely thin atmosphere mostly made of methane, nitrogen, carbon monoxide and oxygen. However, Mars, Triton (Neptune) and Io (Jupiter) present a more substantial atmosphere, thick enough to experience weather variability. On the other hand, Titan - the largest moon of Saturn and the second largest moon of the solar system after Ganymede - exhibit a very thick atmosphere made mostly of nitrogen and methane. Like on Venus, winds and rains are present on Titan which makes its atmosphere very active and more complex.

From all the gas giant planets, Jupiter, the largest one, surely display the most chaotic atmosphere of the entire solar system. The atmosphere of Jupiter is a colourful palette of bands and spots made of sulphur and phosphorus gases. Like on Earth, the Jovian atmosphere possesses clouds, hazes and a weather variability. Its atmosphere is made of several type of clouds with different chemical compounds (sulphur, ammonium, hydro-sulfides) and it is very active: vortices, storms and lightening occur all over the planet. A wide range of

atmospheres already exist within our solar system covering a large spectrum of temperature, pressure, chemical composition and weather variability.

4.1 Detection methods of exoplanets

If such variety exists amongst celestial bodies nearby the Earth, it is natural to ask the question: do exoplanets also exhibit such variety of atmosphere? The answer is yes. But how do we detect an exoplanet and probe their atmosphere? In order to do so, several methods exist. The radial velocity and transit photometry are the two major detection techniques used nowadays.

The radial velocity method also called Doppler Spectroscopy is a method that uses the gravitational effect of a planet on its parent star. An orbiting exoplanet create the star to wobble leading to a doppler shift in the spectrum. The spectrum is blue shifted when the star moves toward us and redshifted when it moves away from us. The more massive the planet and closer to its host star, the larger the star's radial velocity will be. This method will give you the mass of the planet M_p and its inclination.

The second widely used method is called transit photometry. A transit takes place when an exoplanet passes in front of a star relative to the line of sight of the observer. The planet appears as a dark sphere that crosses the stellar disk which leads to a decrease of the stellar flux. The decrease of the brightness will result in a dip in the light curve (see figure 1). The transit depth δ_T encodes the size of the planet with the following equation:

$$\delta_T = \left(\frac{F_{notransit} - F_{transit}}{F_{notransit}} \right) = \left(\frac{R_p}{R_s} \right)^2 \tag{1}$$

R_s is the stellar radius which can be derived from the colour-magnitude relation in stellar models, R_p is the radius of the planet, $F_{transit}$ and $F_{notransit}$ are the incoming flux of the star with a transiting planet and without respectively.

For instance, a Jupiter-like planet $\sim R_J$ transiting a Sun-like star $\sim R_\odot$ will give you a transit depth of roughly 1% ! It is quite obvious that, in order to detect a significant transit, the planet must be sufficiently large compared to its parent star. Detecting transits of much smaller exoplanets are difficult but not entirely impossible, a sub-Mercury-sized exoplanet has been found in 2013 Barclay et al. (2013). Two other measurable quantities can be derived from photometric observations: the transit duration and the period P (characteristic time the planet needs to complete a revolution around its parent star). With those three quantities, one can derive several physical properties of the exoplanet. The shape of the transit can vary quite a lot from one system to another. Indeed, limb darkening moderately affects the shape of the transit curve bottom. This optical effect in stars creates a central peak in brightness and darkened towards the limb. In order to have a viable fit, limb darkening coefficients must be precisely known.

During the transit, if the planet has an atmosphere you can extract the transmission spectra. As the light goes through the planet atmosphere at the day/night terminator, one can analyse the resulting transmission spectra and provide information about the chemical composition. Absorption features can be observed at different wavelengths. The atmosphere might appear opaque, semi-opaque or completely transparent depending on which bandpass one is observing. For example, in the optical range, absorbers are: CH_4, HCN, H_2O, CO, TiO. In the Near-infrared (NIR) absorbers are usually alkali metals: Na, K etc.. In addition, strong absorption features of ionic species can be identified in the UV range and one can probe the exosphere of the exoplanet. Whether the observations are made in the NIR or

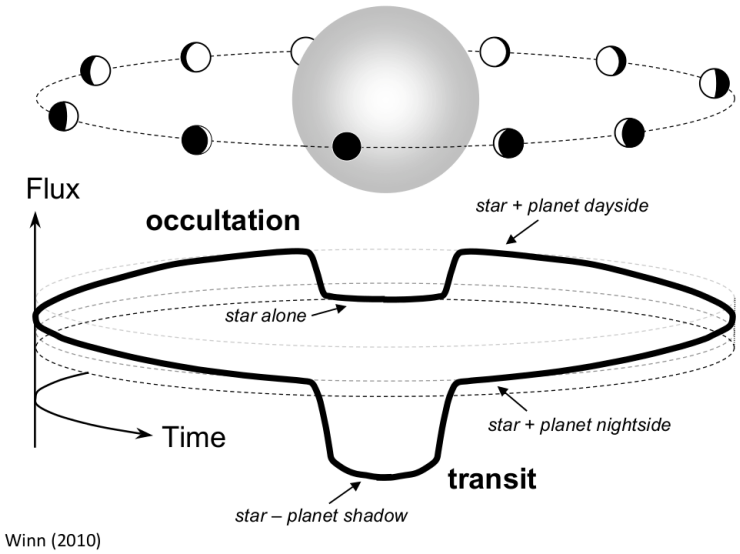

Figure 1: Scheme of a transiting planet

in the Optical, the transit light curve bottom will appear flatter at long wavelengths and curvier at short wavelengths. Even with a thorough analysis and a very high resolution, several caveats remain. Indeed, scintillation and terrestrial atmosphere largely affect ground-based telescope observations. Furthermore, the stellar activity (flares, corona mass ejection or stellar spots) can also alter the light curve significantly.

The atmosphere of an exoplanet can also be characterised through the secondary eclipse. Half of a period later, the planet will disappear behind its host creating another dip in the light curve. However, the dip appears to be much more shallow and less visible than the transit dip. The detection of an occultation is quite challenging for multiple reasons. Like the primary transit the most evident reason is the relative size of the planet compared to its host. Because the eclipse depth is generally 10 to 100 times smaller than the transit depth, one won't even be able to detect it within the noise in the light curve. However, observations with longer exposures can improve the signal-to-noise ratio and a detrending function can be applied to clean up the signal.

Unlike the transmission spectra from the transit technique which gives information about the chemical composition on the atmosphere, the spectra at the secondary eclipse are called emission spectra. They display emission feature characteristics of the day side of the planet. The secondary eclipse depth encodes the thermal emission from the planetary atmosphere and the reflected light from the host star. The thermal emission dominates in the NIR range while the reflection dominates in the optical range. The eclipse depth δ_e can be calculated with the following equation:

$$\delta_e = \left(\frac{R_p}{R_s}\right)^2 \frac{\int B_\lambda T_d d\lambda}{\int B_\lambda T_s d\lambda} + A_g \left(\frac{R_p}{a}\right)^2 \tag{2}$$

R_p and R_s are the planetary and stellar radius respectively. The first part of the right side of the equation corresponds to the thermally emitted planetary component with the

black body B_λ integrated over wavelengths of the planetary day side and the star at the temperatures T_d and T_s respectively Seager & Deming (2010). The second part represent the reflected component with A_g being the planetary albedo and a, the semi-major axis. The secondary eclipse spectra provide precious information about the planetary albedo (bond and geometric) but also about the equilibrium temperature and the day and night temperatures. Furthermore, the chemical composition of the atmosphere on the day side can be extracted within atomic, molecular and ionic emission features. The emission spectra can be very useful in constraining thermal inversion in the atmosphere. Because the day side of the planet is not a homogeneous disk, deviation from thermal and chemical equilibrium frequently cause wrong interpretation of the observations. More details will be explained in the secondary eclipse section.

Both methods have helped us understand the overall structure of an exoplanet from their bulk parameters to their orbital architecture. With the mass derived from the radial velocity and the radius from the transit method, one may estimate the density of the planet. It will help us distinguishing rocky worlds from gas planets.

There are other detecting methods such as direct imaging, gravitational lensing or astrometry. Direct imaging is a method that allow astronomers to take pictures directly of the planets by blocking the light from the star with a coronograph. Gravitational microlensing occurs when the gravity of a massive object will bend and distort the light rays of a distant star. It will temporarily increase its brightness. If a planet is lensed, it will create a distortion during the brighting and dimming event. Finally, astrometry is a method that measure the change in position of the star in the sky compare to reference stars nearby.

4.2 Detection of clouds via secondary eclipse photometry

My research has been focused more on the time variability of secondary eclipses. Indeed, the eclipse depth may vary in time from orbit to orbit due to the presence of clouds in the atmosphere. Some type of clouds, such as silicate or titanium oxide clouds, can form at very high temperature and may be present on the irradiated day side of the planet. However, some other types of clouds may form on the night side when molecules recombine due to lower temperatures and flow toward the day side via the day/night terminator. It is still uncertain how efficient the distribution of clouds from the night to the day side is for tidally locked objects. Some clouds may travel quite a large distance on the day side before molecules dissociate.

Clouds are complex objects because of their fast evolution and intricate physical processes. A deep understanding of atmospheric dynamics and microphysics is necessary. Cloud formation processes depend on several parameters: temperature, pressure, particle size distribution and a balance between rate of coagulation or nucleation and transports. The homogenisation of the temperature in the atmosphere can be understood via the ratio of different timescales. Knowing the dominant aerosol via spectroscopy (transmission and emission spectra) appear to be crucial in understanding atmospheric dynamics and facilitate our interpretation of what types of clouds can form in the atmosphere (silicate, TiO, VO etc).

Clouds and hazes are forming through homogeneous nucleation and photochemistry. They can form and disappear in a very short amount of time making it difficult to trace them. This is why meteorology predictions are fluctuating a lot on Earth. A slight change in temperature or pressure would lead to drastic change of forecast during the same day. The same type of behaviour on UHJ is expected. The section 4 will be dedicated to the

formation of clouds. Overall, a time variability in the eclipse depth would suggest a change in the planetary albedo and therefore a weather variability in the atmosphere of the exoplanet due to the presence of clouds.

There is another technique to probe the atmosphere of an exoplanet called the phase curve which describes the modulation of the brightness as a function of the phase angle. It provides precious information about the thermal structure, day to night temperature contrast or transport processes (aerosols, winds). In the past years, the phase curve method became a powerful tool in understanding atmospheric dynamics. The curve appears with a sinusoidal shape and contains both transit and secondary eclipse. Under some conditions, the secondary eclipse will be located at the maximum point of the curve but most of the time it will be slightly displaced. A secondary eclipse displaced before the maximum point will lead to a shift toward the west of the brightest spot of the planet. On the other hand, if it is displaced after the maximum point, this would lead to a shift toward the east of the brightest spot. The speed of winds can be extracted from the transmission spectrum by measuring the wavelength shift during egress and ingress. However, this is not the topic of this thesis, no detailed information will be provided here.

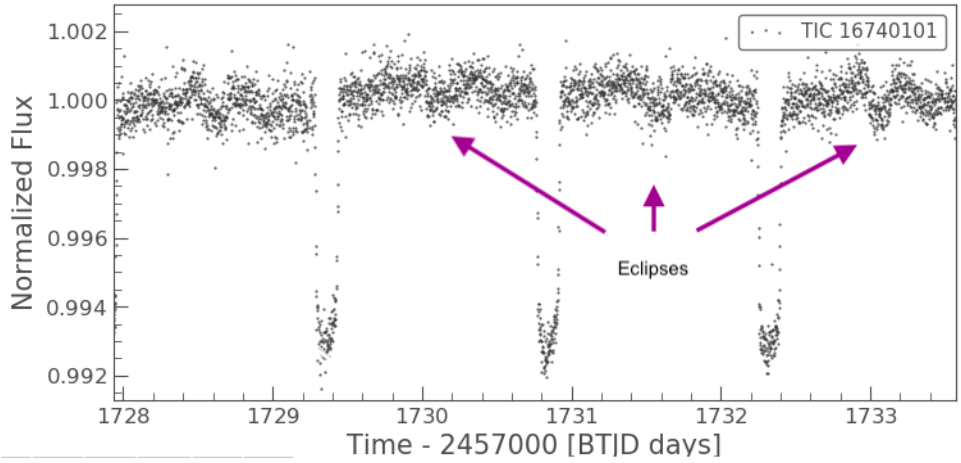

Figure 2: Light Curve of KELT-9b from TESS

Detecting a time variability of secondary eclipses require a sufficient temporal baseline of observation. In order to do so, close-in gaseous giant planets are the best targets. Ultra Hot Jupiters (UHJ) are tidally locked objects with a very short orbital period. They usually have a period of few days and sometimes even shorter than a day in the most extreme cases. Within a few months of observation, a large sample of transits and secondary eclipses can be available. For instance, Wasp18b has been observed for a period of several months scattered throughout two years resulting in 80 secondary eclipses accessible.

This work has been focused on four UHJ which were observed with the Transiting Exoplanet Survey Satellite (TESS). WASP-18b, KELT-9b, WASP-121b, and KELT-1b are the UHJ that I have selected to study time variability of secondary eclipses. The main reason why I have targeted those specific systems is because their eclipses are clearly distinguishable in their light curve (see figure 2). The TESS space telescope was launched in April 2018 and is still running. It was designed to survey 85% of the sky in the solar neighbourhood (400 times more than the Kepler telescope). Originally, it targeted transiting planets with orbital

periods smaller than 10 days with radii $< 2.5\ R_{\oplus}$ orbiting F to M type star. However, a significant number of UHJ has also been detected with TESS.

The most common stars in the Universe are M type star (cool and red), therefore the spectral response function of TESS was designed more toward the NIR range in order to facilitate the interpretation of the emission spectra.

Overall, my research was concentrated on the time variability of the secondary eclipses of four Ultra Hot Jupiters and their physical interpretation. At the time I'm writing this thesis, very few systems display a sufficient and qualitative set of data of secondary eclipses which makes a possible trend rather difficult. On the other hand, I believe that, with the upcoming space missions within the next decade, enormous advancements in the characterisation of planetary atmospheres will be made.

5 Ultra Hot Jupiters, a rising class of highly irradiated exoplanets

Transiting Hot Jupiters (HJ) are unique objects and tend to be more rare than we previously thought. 450 close-in giant gaseous Jupiter-like planets have been found so far with transit surveys. Only 20% have an orbital period of less than 5 days with an equilibrium temperature higher than 500K. Ultra Hot Jupiters are a class of exoplanets which share similar physical and chemical properties with Jupiter, however the major difference between HJ and UHJ lie in their equilibrium temperature: HJ temperatures are lower than 2000K and UHJ temperatures go from 2000K to 4000K for the hottest ones (see figure 3).

UHJ are usually orbiting stars with a spectral type F or G but have also been recently detected around fast rotating A-type stars (KELT-9b Gaudi et al. (2017),KELT-17b Zhou et al. (2016), KOI-13b Santerne et al. (2012)). UHJ orbiting K and M type stars are extremely rare. Indeed ,the level of incoming radiation from cooler stars such as red dwarfs is not sufficient to heat up the planet to very high temperatures. The bulk parameters and the orbital architecture of UHJ are usually well constrained which alleviate the difficulty to characterise their atmospheres. Nonetheless, the understanding of the physical processes behind the formation of clouds on such irradiated planets remains unclear. UHJ are tidally locked objects due to their very close proximity to their parent stars. The orbital period of the planet is synchronous with the rotational period of the star meaning that the same hemisphere of the planet always faces the star. The same mechanism occurs between the Moon and the Earth.

Transmission spectroscopy revealed the presence of absorbers Mallonn & Strassmeier (n.d.) which can be explained by to the presence of high altitude hazes. While the presence of clouds is commonly accepted on HJ, their presence on highly irradiated day sides of UHJ is rather a different matter. The mechanisms involved in cloud formation on UHJ are far more complex.

Only a multi epoch observation of the phase curve at multiple wavelengths Wong et al. (2016) or the time variability of the secondary eclipse depth can suggest the presence of clouds on UHJ. The first technique is privileged since secondary eclipses are frequently absent from transit lightcurve due to the reasons we mentioned in the previous section. Although, the number of UHJ with prominent secondary eclipses has recently increased thanks to the TESS survey.

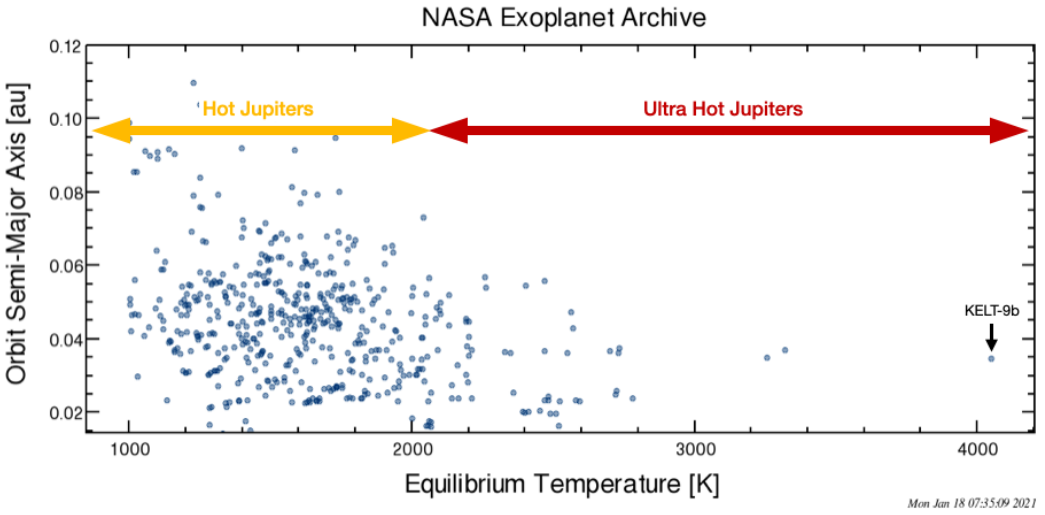

Figure 3: Hot Jupiters vs Ultra Hot Jupiters, NASA exoplanet archive, 2021

5.1 Bulk parameters of UHJ : gaseous, massive and very hot objects

Until today, 30 UHJ have been identified (NASA exoplanets archive) and share similar properties with Jupiter. Masses of UHJ go roughly from $1M_J$ to $13M_J$ the limit mass at which deuterium (an isotope of hydrogen) starts to fuse in the interior. Objects exceeding $13M_J$ are no longer called planets but brown dwarfs. A transiting brown dwarf, HATS-70b, as even been detected at the deuterium burning limit Zhou et al. (2019). The limit mass between brown dwarfs and planets is still an ongoing discussion. Because planets are forming through core accretion and stars through gravitational instability, objects with a mass between $10M_J$ and $13M_J$ do not share the same formation mechanism with planets that have a mass lower than $10M_J$ Schlaufman (2018) and should not then be considered as planets. UHJ exhibit a very high equilibrium temperature higher than 2000K. The hottest ones undergo temperatures up to 4000K.

The planetary equilibrium temperature corresponds to the temperature of a black body heated by the nearby star. It can be expressed as a function of radius and temperature of the star such as:

$$T_{eq} = T_s \sqrt{\frac{R_s}{2a}} (1 - A_B)^{1/4} \tag{3}$$

a being the semi major axis and A_B the bond albedo. The bond albedo corresponds to the fraction of light reflected and absorbed on the planetary surface as function of the phase angle. When the incident light is fully reflected back to space, the bond albedo is close to 0. On the other hand when the light is fully absorbed the bond albedo is close to 1. The bond albedo can slightly differ from the geometric albedo due to atmospheric variation and surface inhomogeneities. The presence of multiple layers of clouds or different cloud species may cause fluctuations in the bond albedo.

Let's take an example of an UHJ orbiting a F type star at a distance of 0.02 AU with $T_s = 6000$K and $R_s = 1.5\ R_\odot$. The corresponding planetary equilibrium temperature with $A_B = 0$ is $T_{eq} = 2500$K. With a bond albedo $A_B \sim 0.3$ due to the presence of reflecting clouds or high altitude hazes, the value drops to 2250K.

Following Cowan & Agol (2011) one may calculate dayside and nightside temperatures of the UHJ as a function of the heat redistribution efficiency ϵ:

$$T_d = T_s \sqrt{\frac{R_s}{2a}} (1 - A_B)^{1/4} (\frac{2}{3} - \frac{5\epsilon}{12})^{1/4} \tag{4}$$

$$T_n = T_s \sqrt{\frac{R_s}{2a}} (1 - A_B)^{1/4} (\frac{\epsilon}{4})^{1/4} \tag{5}$$

The fiducial parameter ϵ value goes from 0 corresponding to no day/night recirculation and 1 corresponding to full recirculation. UHJ display frequently a high temperature contrast between the two hemispheres, sometimes more than 1000K. A possible correlation can be found in Keating et al. (2019) between T_{eq} and ϵ. Indeed, with increasing T_{eq} up to 2500K, ϵ is decreasing meaning that recirculation on UHJ is not very efficient. However, there is an evidence for H_2 dissociation and recombination in KELT-9b Mansfield et al. (2020) proving that the balance between cooling and heating from these processes improve the overall energy redistribution on the planet. This can be reflected on a smaller amplitude on the phase curve, indicating an efficient heat transport.

5.2 Peculiar orbital architecture with a short periodic signature

UHJ have a short periodic signature. So far, less than 40 UHJ exhibit an orbital period of less than 5 days (NASA Exoplanet Archive) and only 5 are Ultra short period planets (USP) with an orbital period lower than 1 day (KELT-16b, WASP-18b, WASP-103b, WASP 19b and HATS-18b). Because of their proximity to their host stars, UHJ are most likely to have circular orbits or extremely low eccentric ones (e $\sim 10^{-3}$). Objects with very short orbital periods are ideal objects in order to constrain the planetary parameters. Indeed, a consequent temporal baseline of observation facilitate the interpretations.

UHJ orbit extremely close to their host: between 0.01 and 0.05 AU. This proximity causes the planet to be in tidally locking which leads to quite an exotic configuration. A permanent extremely irradiated day side where chemical compounds are in atomic and ionised states and a permanent night side where a lower temperature allows molecules to recombine and condensate.

5.3 Formation and evolution of UHJ

The topic of the formation of HJ and UHJ is still under discussion in the planetary formation community. Indeed, those exotic gas giants should have not formed in the same location as their current orbit. In principle, the planet should form much further away in the protoplanetary disk beyond the ice line, migrate toward the central star and park on a tidally locked orbit Lothringer et al. (2020) In the early phase of the protoplanetary disk, the planet form by core accretion and because of its interaction with the surrounding material, the original orbit will be altered. Once the solid core is large enough, the planet will form a gaseous envelope when the gravitational drag is sufficiently strong.

During this process the planet may accumulate enough material to reach a mass of several Jupiter mass. HJ are subject to a migration of type II. While the migration of type I targets planet with a lower mass, the type II create a gap in the debris disk around a massive planet. It appears that no distinction has been made between UJ and UHJ regarding the physical mechanisms involved in their formation. Other hypothesis have been also discussed to understand the origins of HJ (in situ or tidal migration) and how can they match the actual observations. They are very well summarised in Dawson & Johnson (2018) published in January 2018.

5.4 Atmospheric characterisation of UHJ

Observations of UHJ atmospheres through ground and space surveys have largely increased in the recent years. A massive amount of work is on the way to understand the physical processes behind the exotic atmosphere of those peculiar and unique planets. In order to have a global view of UHJ atmospheres a large sample of discipline is involved: micro-physics, atmospheric dynamics, chemistry and many others. Atmosphere of UHJ are complex and somewhat unpredictable due to the disordered and turbulent space weather around them. There are no similar objects in our solar system to compare these objects to. Extensive computational models have been developed to explain such patterns and match the observations. Plenty information about UHJ have been gathered and lighten the characterisation of their atmosphere.

5.4.1 Dynamics

The understanding of atmospheric circulation and dynamics on UHJ has increased tremendously lately and had reduced the difficult task of their characterisation. Indeed, 3D General Circulation Models (GCM) for example have been developed and are powerful tools to simulate the dynamics of a planetary atmosphere. GCM incorporate several levels of mechanisms from chemical composition to the balance between radiative cooling and dynamics.

These models have successfully reproduced the strong-rotating equatorial jet on UHJ producing a shift of the hottest point of the planet eastward or westward of the substellar point. Indeed, the occultation (secondary eclipse) may be drifted from the maxima point while the transit may be displaced from the minima point. The phase curve provides not only the longitude brightness but also information about the thermal structure of the planet.

Hydrodynamic transport processes such as advection or winds can drive the energy either horizontally from the day side to the night side or vertically from equator to pole. The advective timescale at which the characteristic time for a parcel of gas to move horizontally is given by:

$$\tau_a = \frac{R_p}{U} \tag{6}$$

R_p being the planetary radius and U the wind speed Showman & Guillot (2002). UHJ due to their extremely high temperature have a very short radiative timescale. The radiative timescale is the characteristic time for a parcel of gas to loose its energy through radiation given by:

$$\tau_r = \frac{PC_p}{g4\sigma T^3} \propto \frac{1}{T^3} \tag{7}$$

P being the pressure of the photosphere, Cp the heat capacity, g the surface gravity, σ the Stefan Boltzmann constant and T the temperature. In the case of UHJ, the characteristic radiative timescale is very short $\sim 10^4$s and much smaller than the advective timescale. This means that UHJ have a large day to night temperature contrast. Their atmosphere will cool down before dynamics dissipate the energy. Furthermore, one may calculate the zonal wind speed on UHJ using the thermal wind equation Vallis (2017). Drag forces are generally neglected on UHJ and a typical value of 2 to 4 km/s is found for the zonal wind speed. Some physical processes may drive away the homogenisation of the temperature and lower the temperature gradient on UHJ. The energy needed to dissociate molecular hydrogen may cool down the irradiated hemisphere.

On the other hand, the energy released due to molecular recombination may on the contrary heat up the night side. In addition, UHJ undergo strong tidal forces from their parent stars which heat up their interior and may have a significant impact on the atmosphere. The connection between interior and atmosphere of close-in massive planets is still poorly understood. Some UHJ may even present radii much larger than expected such as WASP-121b Delrez et al. (2015). Diverse explanation have attempted to explain these inflated UHJ: tidal stellar dissipation Bodenheimer et al. (2001) or vertical advection of potential temperature Tremblin et al. (2017). Another aspect that has been put aside for a long time is the effect of the Magnetohydrodynamic drag and the magnetic field on atmospheres. The substantial thermal ionisation present on UHJ atmosphere may have a serious consequence on dynamics.

5.4.2 Atmospheric chemistry

The chemical composition of planetary atmospheres can reveal serious clues on the physical processes of those extreme worlds. The chemistry characterisation of UHJ and UJ atmospheres has accelerated in the past years. Because of their tidally locking and their very high temperature most species present on the day side are either ionised or on the atomic level. On the other hand, species may appear in the molecular level on the night side where the temperature is sufficiently low to allow molecular recombination and condensation. Knowing the relative chemical abundance of each element present in the atmosphere is an important step of the chemistry characterisation.

In fact, transit spectroscopy is the most efficient method to do so and has enabled us to reveal neutral and ionised elements like C, N, O, Mg^{++}, Si^{+}, K and molecules like H_2O, CO. More recently, transmission spectroscopy of several UHJ have revealed broad absorption features of H_2O in NIR for example in WASP-12b Kreidberg et al. (2015) or the presence of more exotic species such as Titanium Oxide (TiO) in WASP-19b Sedaghati et al. (2017) (see figure 4).

The atmosphere of UHJ is stratified on both hemispheres. Deep into the atmosphere, the composition is mostly governed by chemical equilibrium, one of the main assumption of GCMs. Notwithstanding, various physical mechanisms drive out from chemical equilibrium in upper layers of the atmosphere. Photochemical reactions caused by the strong UV irradiation from the parent star are expected to dominate on the day side of UHJ. Indeed, the incident stellar flux interacts with the molecules present in the atmosphere and will photodecompose (the same mechanism occurs in the Earth ionosphere). Disequilibrium can also be caused by another chemical kinetic effect due to vertical mixing: quenching Moses (2014).

The chemical quenching can affect the opacity at several wavelengths significantly. The

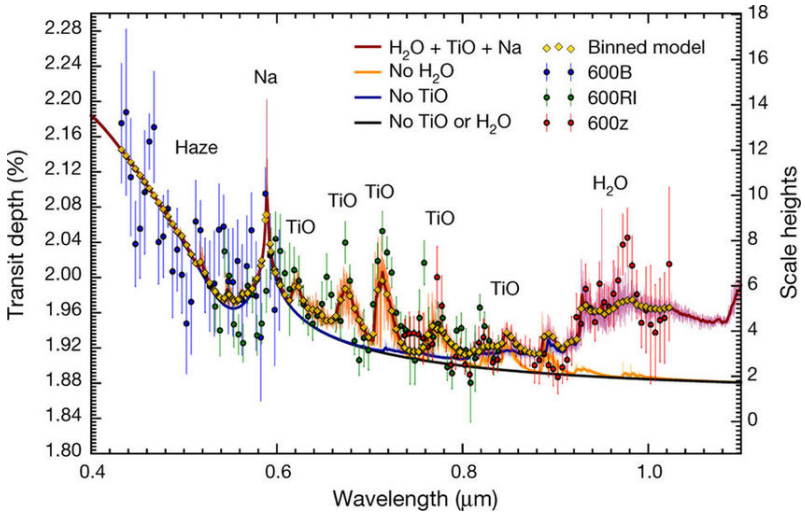

Figure 4: Transmission spectrum of WASP-19b showing TiO, Na and H_20 features

very high ionisation of metals and the thermal dissociation of molecules in the irradiated side of UHJ constitute the major source of e^- responsible for the H^- opacity. The relation between the metal abundance and the H^- continuum is pretty straightforward. An increasing metallicity leads to a larger fraction of e^- available and will increase the opacity. Very massive UHJ in principles have a metallicity very close to their parent star.

The presence of thermal inversion (red line in figure 5 Madhusudhan (2019)) in planetary atmosphere is a very common feature but remain an opening question for UHJ. The existence of TiO and VO may be the cause of the thermal inversion in UHJ due to their capacity to absorb incident stellar light Gandhi & Madhusudhan (2019). However these molecules remain quite difficult to detect as, for example, in the atmosphere of WASP-121b Merritt et al. (2020).

5.4.3 Cloud formation processes

The variety of clouds/hazes within our solar system is quite substantial. The atmosphere of Jupiter is composed mainly of ammonia clouds (NH_3). Venus displays sulphuric acid clouds (H_2SO_4) and Titan's clouds (Saturn's largest moon) are mostly made of methane (CH_4). Nonetheless, the formation or the existence of clouds on UHJ remain a burning question. If theirs day sides may appear cloud-free because of the the extreme irradiation, the climate on night sides is more propitious to cloud formation.

A damping of spectral features in the spectra and a change in the amplitude of the phase curve are symptomatic of the presence of clouds Parmentier et al. (2021). Moreover, the large umbrella of cloud species may explain why such a variety of phase curve is observed. In addition, the optical phase curve can probe the planetary albedo. Night clouds may spill over to the day side through the day/night terminator and become reflective clouds, increasing the scattering light present in the optical band.

Clouds undergo rapid changing processes, they form through homogeneous particle nucleation, condensation and transport via sedimentation. A deep understanding of microphysics is necessary to comprehend properties of clouds. Cloud particles (aerosol) are made

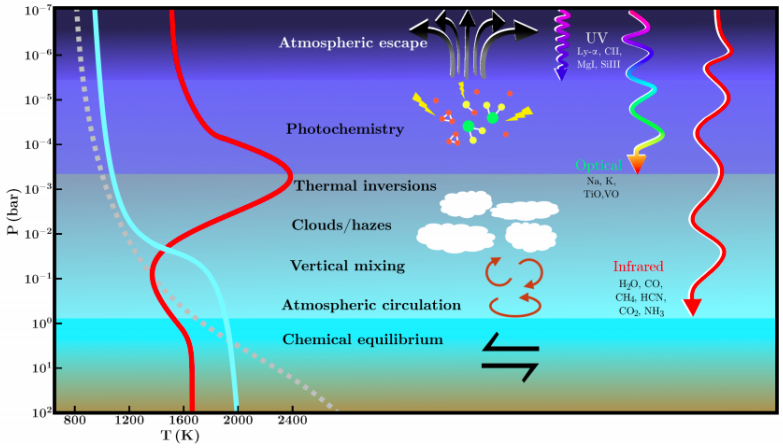

Figure 5: Physical and chemical processes in UHJ and UJ atmosphere

of microscopic chemical compounds in the solid or liquid state. Haze particles are however produced through photochemical reactions and are much smaller in size. Knowing the dominant aerosol via spectroscopy (transmission and emission spectra) is crucial to facilitate our interpretation of what type of clouds are forming on UHJ.

Recent publications may lighten the debate on the type of clouds that can be formed on UHJ. An atlas of aerosol composition of HJ has been proposed Gao et al. (2020). They modelled a 1D microphysic model taking into account temperature, metallicity and surface gravities. They found that the amplitude of the silicate spectral feature is quite prominent and that titanium oxide condenses for hot planets with $T_{eq}\sim$ 2000K, meaning that silicates and TiO clouds can indeed form on UHJ.

Furthermore, the metallicity goes hand and hand with the cloud formation: the higher the abundance of metals in the atmosphere the more likely clouds will form. Clouds can also be detected via the evaluation of climate variability through multi epoch eclipse observations Kilpatrick et al. (2020).

The objective of this work is to seek for secondary eclipse depth variability of UHJ which is a symptom of a change of the albedo. This fluctuation could be a clear evidence of a cloud coverage on the day side of the UHJ. Because of the flaw of secondary eclipse observations, very few studies and observations has been made to characterise weather variability on UHJ. The analysis of the phase curve of Kelt-1b may suggest a high dayside albedo which could be due to the presence of silicates clouds Beatty et al. (2020). However, no hints of reflective clouds have been found in the report of low albedos of UHJ in the optical to NIR Mallonn et al. (2019).

6 Data reduction

6.1 Transit Exoplanet Space Survey (TESS)

UHJ are expected to exhibit climate variability and in order to investigate this weather fluctuation I have used the data from the Transit Exoplanet Space Survey (TESS) launched in 2018. Its primary mission was to survey stars with a spectral types from F5 to M5. It searches a large sample of transiting exoplanets with periods <10 days and radii <2.5 Earth radii orbiting bright stars Stassun et al. (2018). While Kepler was designed to survey a small portion of the sky, TESS is able to monitor up to 80% of the sky in the solar neighbourhood (<60 parsecs). TESS is mounted with four CCD cameras creating a 96x 24 degrees field of view. Each Earth hemisphere was observed for 1 year, totalising 26 sectors in 2 years of observations Ricker et al. (2014).

Because the primary goal of TESS was to observed mostly M stars which are most sensitive to red wavelengths (most common stars in the solar neighbourhood), its bandpass was manufactured within the NIR range. Its spectral response function (see figure 6) has a maximum quantum efficiency (QE) from 600 to 1000nm, covering R_c, I_c and z filters Ricker et al. (2014). Charge coupled device (CCD) detector was invented at the end of the 60's and revolutionised observational astronomy surveys and photometry due to lower noise and very high QE at high wavelength. Photons are collected by a pixel element and convert into an electrical potential (a signal) which can be directly processed by computers.

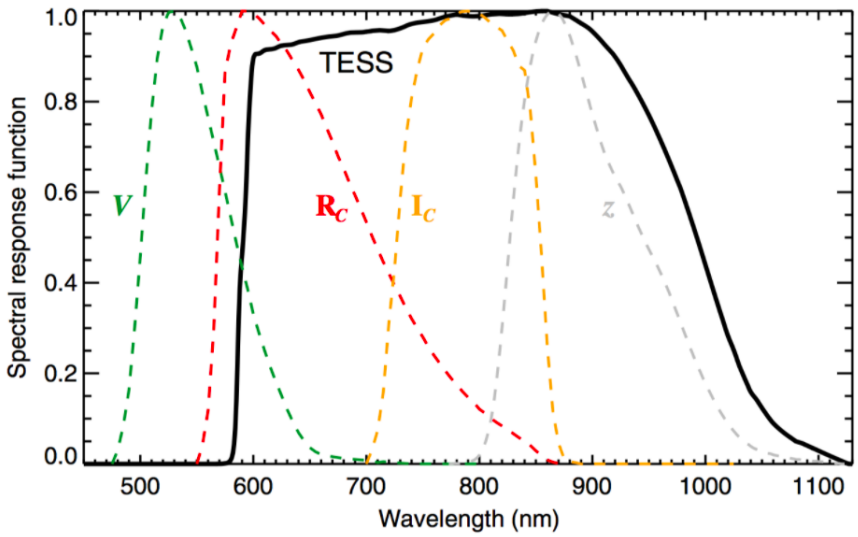

Figure 6: Spectral response function of TESS

The extended mission has started in July 2020 and will continue to seek for transiting exoplanets until July 2022. A 10-minute cadence will be assigned for the next two years of observations instead of a 30-minute full frame images (FFI). This result as a larger sample of data points in the light curve (see the results section).

6.2 Data access and analysis

6.2.1 Data products

Full frame images (FFI) are a compilation of pixels observed at the same time. For each given orbit, 900 2-seconds full frame integration are converted into 30-minute FFI which gives up to 600 30-minute FFI from each individual camera Ricker et al. (2014).

Target Pixel Files (TPF) are the unprocessed form structure of the target (the star), see picture 9. Photometry can be performed either on uncalibrated or calibrated data. Multiple TPFs can be generated in the case of multiple observations through different sectors. WASP-18b has for example 4 different TPFs available since it was observed in 4 different sectors. They can either have a 2 minute or 20 second cadence. However, only cycles 3 and 4 of the survey provide 20 second cadence TPFs. The TPFs display the Flux in $e^{-}s^{-1}$ with the Pixel row and column number (see figure 8). All TPFs of the selected targets can be found in the Appendix.

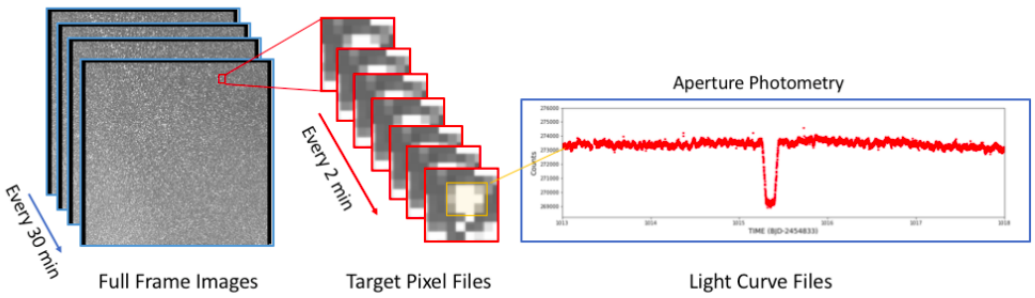

Figure 7: TESS data products

Finally, Light Curve Files (LCF) can also be created using Simple Aperture Photometry (SAP) meaning that all pixel values are added in a pre-defined aperture as a function of time (see figure 7).

The sector of a given target can be found using the Web TESS Viewing Tool (WTV) either by its name (ex : WASP-121b), by its TESS Input Catalog (TIC) Stassun et al. (2018) (ex : TIC 22529346) or by its coordinate : right ascension (RA) and declination (DEC). An estimation of magnitude and photometric error for a point source given known magnitudes is also possible by giving the set of stellar magnitudes.

FFIs, TPFs and LCFs are all available on the Mikulski Archive for Space Telescopes (MAST) and can be downloaded in Fits format. Once you've entered a target, several information can also be found on MAST archive : Instrument, filters, waveband, target name, ID, coordinates and exposure length.

I have also used the EXO.MAST (https://exo.mast.stsci.edu/) archive where MAST(https://archive.stsci.edu/) data can be found with Plot sector-stitched DV light curves, exoplanet parameters with their references and Data Validation Reports for TESS TCEs. This archive can be very handy to have a quick check of the last papers that refer the orbital and stellar parameters needed for the analysis of my targets.

6.2.2 Lightkurve package

The Lightkurve package is a Python-based tool which was developed originally for the KEPLER mission and later on for the TESS survey Cardoso et al. (2018). This package is a straightforward window to extract all data products from TESS, creating light curves using aperture photometry and correcting systematics. Indeed, systematic errors in differential photometry which can be caused by uncalibrated flat fields which happen regularly with CCD detectors.

Appart from constructing a light curve from a TESS observed object, one may also build up a periodogram to identify periodic signals and rotation rates. At last, an estimation of the mass and the radius of the star can also be achieved via asteroseismology with this tool.

In order to extract the lightcurve, I have used jupyter notebook, a web based interactive computing notebook environnement provided by Anaconda Navigator. The procedure to extract the light curve for an object is the following (let's take KELT-1b as an example) :

First step : I searched for the light curve fits file using the Pre-search Data Conditioning SAP flux (PDCSAP) procedure which is usually cleaner than Simple Aperture Photometry flux (SAP) by computing the name of the object, the mission and the sector (with WTV), see figure below. PDCSAP photometry creates basis vectors from selected regions of the field-of-view that describe the components of the most common photometric variations across multiple channels. These are then fitted and removed from the data Plachy et al. (2019).

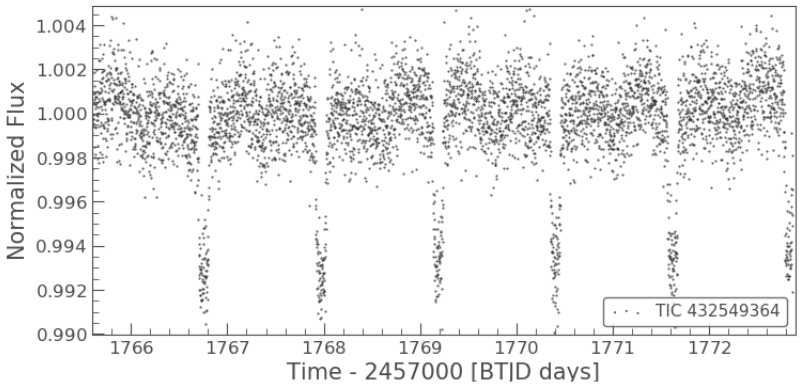

Figure 8: Extracted lightcurve, normalized flux vs time

Second step : I downloaded the TPF by the same command by entering the name of the target, its sector and its cadence (short for 2 min and long for 30 minute). This gave me : TessTargetPixelFile(TICID: 432549364), see figure below.

Third step : I've downloaded the TPF time arrays at each cadence which will be needed for a viable fit. The TPF time is displayed as counted since Julian Day 2457000. Other functionalities can be applied to the light cuve such as : removing outliers, removing long term trend (if the curve appears inclined), folding the data and finally reducing the time resolution (bin).

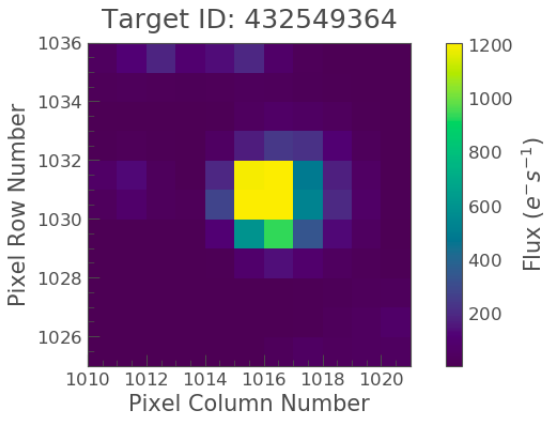

Figure 9: Example of a TPF file of WASP-18b

6.3 Target selection

The criteria to select the targets were the following :

1. An equilibrium temperature higher than 2000K
2. An orbital period of less than 2 days.
3. A semi major axis lower than 0.05 AU.
4. A mass greater than 1 M_J
5. At least 5 secondary eclipses must be significantly visible in the light curve.

Indeed, in order to detect a temporal variability on a large baseline of observations, a comfortable number of eclipses must be present in the light curve. Some attempts have been unsuccessful primary because of the lack of secondary eclipses available Kilpatrick et al. (2020). These criteria lead to the selection of four objects : KELT-1b, a brown dwarf of 30 M_J, KELT-9b the hottest exoplanet ever found orbiting an A0-type star, WASP-18b the most well studied UHJ and finally WASP-121 which also display a significant number of eclipses. Both WASP-18b and WASP-121b have been observed twice which increase our chances to detect climate fluctuations from orbit to orbit. A 2 years gap between the first and the second set of observations is however present for both targets.

6.4 Model Fitting and Detrending strategy

6.4.1 Modelling

Each individual eclipse was fit with a Mandel & Agol Model. This model was initially developed for transiting planets by Kaisey Mandel, Eric Agol in 2002 Mandel & Agol (2002). They modelled the planet as dark sphere transiting a stellar disk following quadratic or linear limb darkening laws. They compute an analytic function for transiting light curves following the limb darkening laws. Including the limb darkening has been crucial to have a viable fit since the stellar disk does not appear as an homogeneous bright sphere. The disk peak in brightness in the center and gets darker toward the edges. They enumerated several cases regarding the position of the planet compare to the star, from the case where the star is unobscured, to the case where the planet lies in the limbs or the case where the planet is

near the center of the stellar disk. For each individual case, the flux has been determined with respect to the space parameters.

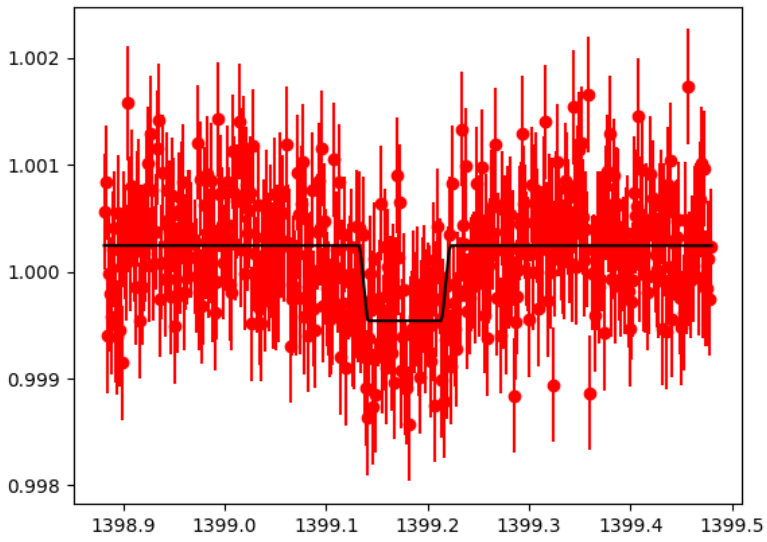

Figure 10: Fit on one single eclipse of WASP-18b

In our case, the limb darkening is not taking into account since we analyse the secondary eclipse, when the planet disappear behind the star. Following, von Essen et al. (2019), to fit the eclipses, I scaled the canonical primary transit model by setting the limd darkening coefficients to zero and the secondary eclipse depth is calculated as the following :

$$SEM(t) = (TM(t) - 1) \times sf + 1 \tag{8}$$

Where TM(t) correspond to the transit model and SEM(t) the secondary eclipse model. Sf is the scaling factor which preserve the parameters of the transit that can be derived via the fit. Since both transit and secondary eclipse phenomena depends on the same parameters. Then, we have :

$$\delta_e = \left(\frac{R_p}{R_s}\right)^2 \times sf \tag{9}$$

Each fit is computed with its own error propagation.

The stellar, orbital and planetary parameters were used as input fixed parameters within the model. One may consider the values of those parameters from the literature as starting values, preferably the most recent publications for a better fit. In our case, all parameters are fixed except the scaling factor parameter.

I have used the flatten function with a window length of about 5% of the total dataset to flatten the light curve. The light curve has been then folded using the period and the mid-time transit. The transit mid-time Tmid needed for the fit is explained in Alexoudi et al. (2018) as the following :

$$Tmid = T_0 + P \times nc \tag{10}$$

nc being the corresponding cycle number of the reference mid-time.

The list of the fixed parameters is the following : orbital period P (in days), the inclination i (in degrees), the semi major axis scaled in stellar radius a/R_s, the planet-to-star radii ratio R_p/R_s, the linear and quadratic limb darkening coefficients, the eccentricity and the orbital elements Ω (the ascending node of the ellipse) and ω (argument of the periapsis). The assigned valued of the secondary eclipse model are set for a Keplerian orbit.

A quick fit is first established to have a preliminary view of what it may look like (see figure 10 above).

6.4.2 Detrending Function

The detection of secondary eclipse events undergo several caveats and observational challenges. They are very difficult to detect because of the small size of their depth compare to the transit ones. Due to geometrical consideration (i $< 70°$) the eclipse event may not occur. However, our UHJs have an inclination close to 90° and display a quasi-circular keplerian orbit meaning eclipse events will take place and may be seen in the lightcurve. Moreover, observations are made from a space telescope leading to no perturbations caused by the atmosphere of the Earth (airmass, seeing).

The stellar activity (presence of spots) or instrumental effects of the telescope may cause systematics (long term trends in the light curve). Those low-level systematics can be removed using a detrending strategy by fitting a detrending polynomial function. The detrending model is detailed in von Essen et al. (2018). In our case only the first and second order of the model have been used. It has the following expression :

$$DM_t = a_0 + a_1 DM_{t-1} + a_2 DM_{t-2} \tag{11}$$

With a_0, a_1 and a_2 being the detrending coefficients,DM_{t-1} and DM_{t-2} being first and second order of the polynomial. We have now a model which combine a scaled version of Mandel & Agol model with a detrending strategy which can be used to fit each individual eclipses.

6.5 MCMC and Steppar procedure

6.5.1 MCMC

After the preliminary sketch (figure 10), I performed the fit with a Markov Chain Monte Carlo (MCMC) procedure. This algorithm has been widely used in the field of observational astronomy to derive the orbital parameters of an exoplanet for example. The Monte Carlo describe is a statistical tool sampling a probability distribution and approximating a chosen quantity (in our case, either the scaling factor for the secondary eclipse or the ratio Rp/Rs for the transit). The Markov chain generate a chain of arbitrary variables where each newly variable generated is dependent upon the previous one Brooks et al. (2011). The extracted light curve (the input) would go through the MCMC process and generate a set of sample of posteriors as output. In addition, one may obtain a reasonable estimation of the best fit as a by-product.

The higher number of free parameters you have within your MCMC procedure, the longer it will take to process. In our case, only four parameters (sf or Rp/Rs, a_0, a_1, a_2) were set as free and the rest were frozen (inclination, semi major axis).

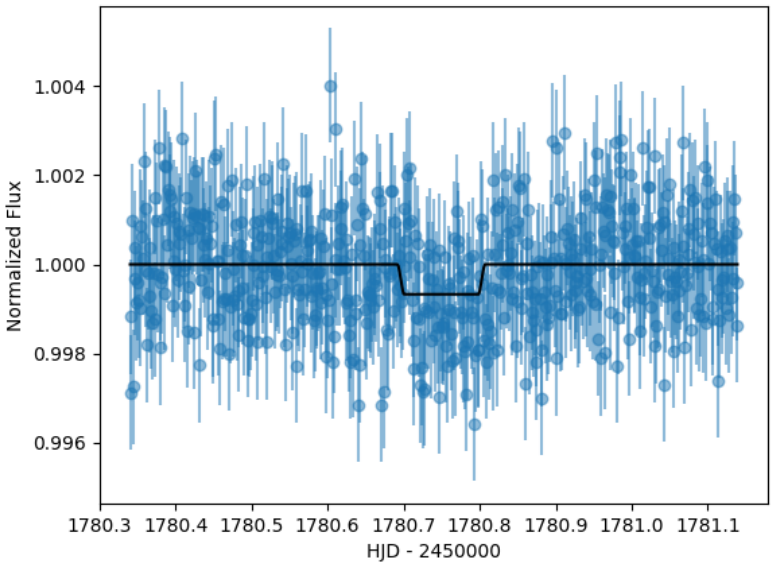

Figure 11: MCMC procedure performed on one eclipse of KELT-1b

I ran multiple chains length independently (10,000 ; 25,000 ; 50,000 ; 100,000 and 200,000) to make sure the value was converging nicely at the same end point. The length of each chain was set to 50,000 steps with a burning phase of 20%. The burn-in steps correspond to the initial steps that try to reach your final solution and need to be cleared out to get a better sample of posteriors. Uncertainties for each free parameters are given for each individual chain. Several hours are needed to run a MCMC procedure for a single eclipse or a single transit. You may see on figure 11 the resulting plot of a single eclipse of WASP-18b after a MCMC procedure.

6.5.2 Steppar command

We expect to have high standard deviation values for each individual eclipses. However, the MCMC procedure did not match our expectations and rather gave us smaller standard deviations values per eclipse. The reliability of the uncertainties depends either on the data treatment (outliers), on the model itself or on the number of free astrophysical parameters. Most parameters were frozen during the MCMC procedure. In oder to have more reliable uncertainties, I had to performed the ft with a second statistical tool called Steppar. The Steppar command is available via the Pyastronomy package. It is used to determine a confidence interval of your parameters.

I had to modify the script and replace the MCMC procedure with the Steppar command. The fixed parameters remain unchanged except for the detrending coefficients which have been frozen due no strong variations on the polynomial present in the fit. For most of the

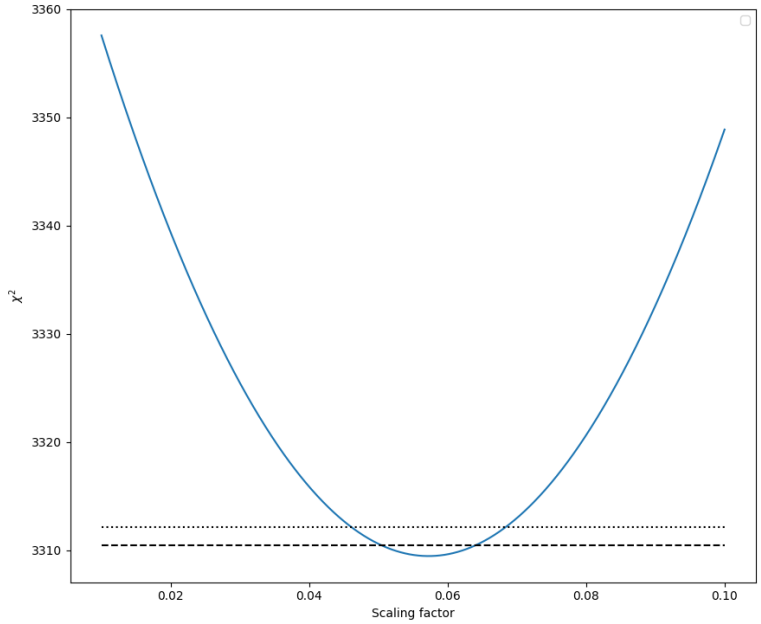

Figure 12: Example of a chi square statistic for 1 eclipse, KELT-1b

eclipses the polynomial structure is well behaved. Only the scaling factor is thawed during the stepping.

The χ^2 statistic basically describe how good the model fits the data. Because I work with time-series photometry (no repeatable data), the χ^2 statistic can be used here. It has the following equation:

$$\chi^2 = \sum_{i=1}^{N} \left(\frac{x_i - \mu_i}{\sigma_i} \right)^2 \tag{12}$$

$\mathrm{x}_i \pm \sigma_i$ correspond to the data and μ_i to the model. The confidence levels for the interval of our values are set to 90% and 68%, dashed and dot lines respectively. Each procedure was performed with 1000 steps. The figure 12 shows the confidence interval for the normalisation of a Gaussian for 1 eclipse of KELT-1b. The new standard deviation for each individual eclipse is calculated as the following :

$$\sigma = \frac{\sigma_{max} - \sigma_{min}}{2} \tag{13}$$

σ_{max} being the largest parameter value and σ_{min} the smallest parameter value of the confidence interval.

6.6 Spearman rank coefficient

The Spearman's rank correlation coefficient r_s describe the statistical dependance between two variables. Those two variables in our case correspond to the transit and secondary eclipse depths. Because our type of data are two independent and continous variables we want to test a possible association between the two variables.

This non-parametric method is working under several assumptions : two variables are needed, both variables are rank-ordered and must have a monotonic relationship. The spearman coefficient would then describe a linear association between the ranks of the variables Siegel (1957).

It has the following expression :

$$r_s = 1 - \frac{6 \sum {d_i}^2}{n(n^2 - 1)} \tag{14}$$

n correspond to the number of observation and d_i = rg(X_i) - rg(Y_i) is the difference between the ranks of each individual observation. X_i and Y_i are one pair of observation corresponding to the eclipse and the transit depth respectively. The value of the spearman coefficient goes from +1 meaning that for each increase in X axis you would have an increase in Y axis leading to a positive correlation. On the other hand, a value of the coefficient close to -1 would lead to a negative correlation (or anti-correlation).

A value close to zero implies no association between the ranks. This additional statistical analysis may indicate a possible positive or negative correlation between our set of data and may lead to a stronger evidence of a real detection of climate variability. Indeed, if the spearman rank coefficient has a value close to 0 for 1 system, it would suggest that the transit depth variability and the secondary eclipse variability are not correlated. On the other hand, a strong correlation or anti-correlation may suggest that the transit depth and secondary eclipse variabilities are somewhat related. Either way the secondary eclipse depth variability is caused by the stellar activity or by systematics.

In order to test if the results occurred by chance or not, a p-value is associated to the spearman coefficient. While a low p-value (below 0.1) meaning that the results did not happen by chance, a very high p-value would suggest otherwise. This p-value gives you the the probability to see this correlation value randomly without physical connections (spots etc.). The data become valid with a very low p-value meaning the more reliable our correlation is (positive or negative).

7 Results

7.1 KELT-9b

Kelt-9b discovered in 2017 Gaudi et al. (2017) is the hottest exoplanet ever found. With an equilibrium temperature of 4000 K, this UHJ is hotter than most stars in the Universe : K and M type stars! The lower temperature limit of UHJ is set around 2000K. However, no upper limit has been yet fixed for this class of exoplanet mostly because no exoplanets with $T_{eq} > 3000$K were found before Kelt-9b.

KELT-9b orbits a fast rotating A0V/B9V star with a temperature of 10140 K. Exoplanets orbiting such type of star are very rare, so far, only 5 of this type are listed. It has a day side temperature of more than 4500K and a night side temperature of 2500K Mansfield et al. (2020) which result a very large temperature gradient of more than 2000K between its two hemispheres.

This extreme irradiated gas giant pushes boundaries in several physical mechanisms from atmospheric dynamics to photo-evaporation or even to its own formation. Indeed, Kelt-9b receives between 500 to 1000 times more ultraviolet radiation than most UHJ known leading to exotic photochemistry on its day side. Moreover, the extreme insolation from the nearby start Kelt-9 causes the planet to have an inflated radius and a poor heat redistribution predicted by models. Nonetheless, strong evidence of H_2 dissociation and recombination between both hemispheres impact strongly the energy redistribution Mansfield et al. (2020). This process would partially explain the relatively low amplitude of the phase curve of Kelt-9b.

Because of the extreme regime that KELT-9b undergo, one may expect a total dissociation of molecules on its day side contributing, inter alia, on a H^- continuum opacity. We may also expect a featureless emission spectra from its day side.

Parameters	**Description**	**Value**	**References**
M_s	Stellar Mass	2.52 $M_\odot \pm 0.2$	Gaudi et al. (2017)
R_s	Stellar Radius	2.36 $R_\odot \pm 0.07$	Gaudi et al. (2017)
[Fe/H]	Metallicity	-0.03±0.2	Gaudi et al. (2017)
T_{eff}	Effective Temperature	10170K±450	Gaudi et al. (2017)
RA	Right Ascension	20:31:26.376	
Dec	Declination	+39:56:20.10	
M_p	Planet Mass	2.88 $M_J \pm 0.84$	Gaudi et al. (2017)
R_p	Planet Radius	1.891 $R_J \pm 0.05$	Gaudi et al. (2017)
T_{eq}	Equilibrium Temperature	4050K±180	Gaudi et al. (2017)
log g	Surface Gravity	3.3002	Gaudi et al. (2017)

Table 1: Kelt9 Ephemerides, stellar and planetary parameters

It is predicted that clouds cannot form on its day side but molecules may recombine and condense on its night side forming clouds and hazes. They may travel toward the day side via the terminator but due to the extreme incoming radiation they will rapidly disappear. Kelt-9b is an incredible laboratory to understand the extreme cases and limits of numerous chemical and physical processes present in its atmosphere.

More recently, they traced molecular features on the emission spectrum of Kelt-9b Changeat & Edwards (2021) contradicting with a featureless spectrum in the NIR that

model would predict for such UHJ. Indeed, they found relative high abundances of optical absorbers : TiO, VO and FeH. Vertical mixing may be responsible for a more stable and cooler region in the atmosphere where such molecules can exist.

However, those molecules may also be leftovers from nightside clouds that have traveled on the day side. We have seen that TiO clouds can form and survive at very high temperature and may be one of the possible explanation that cause a variability in the secondary eclipse depth.

System	**Description**	**Value**	**Literature**
Per	Orbital Period	1.481109±3.5e-6	Wong et al. (2020)
R_p/R_s	Ratio Radii	0.08±0.002	Ahlers et al. (2020)
i	Inclination	87.2°±0.4	Ahlers et al. (2020)
a/R_s	Semi major axis	3.15±0.0093	Wong et al. (2020)
Transit			
u_1	Linear Limb Darkening	0.1588	Ahlers et al. (2020)
u_2	Quadratic Limb Darkening	0.2544	Ahlers et al. (2020)
T_0	Transit Midtime	1683.449±0.001	This work
Eclipse			
Sf	Scaling Factor	0.11±0.05	This work
T_0	Eclipse Midtime	1684.185±0.001	This work

Table 2: Starting values of the system for the fit

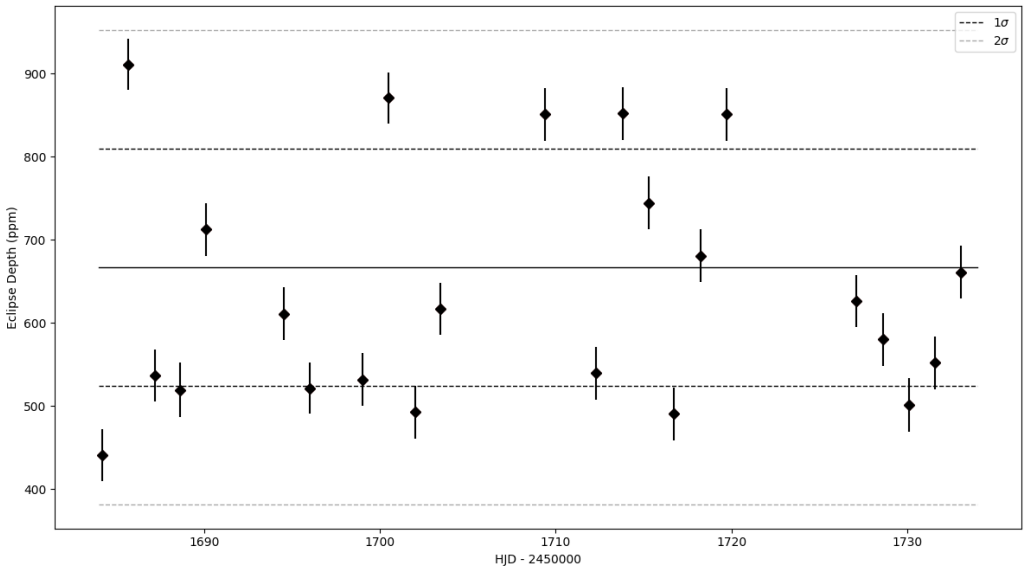

Figure 13: Secondary Eclipse Depth and timing for Kelt-9b

Here I present the results of the best fits of the secondary eclipses and transits of Kelt-9b. The extracted light curves are found in figures 31 and 32 in the Appendix. Table 1 lists all the stellar and planetary parameters of Kelt9 and its planetary companion taken from

EXO-MAST archive. Table 2 lists all the parameters needed for the fit of each individual eclipse and transit. A total of 23 eclipses and 24 transits have been analysed both with an MCMC and a Steppar procedure. Because both displayed similar results for the standard deviations of each individual eclipses, I only choose to show the results from the Steppar procedure. The results are listed in table 9 & 10 along with their uncertainties and the time (note that the real time correspond to the AOR + HJD 2450000).

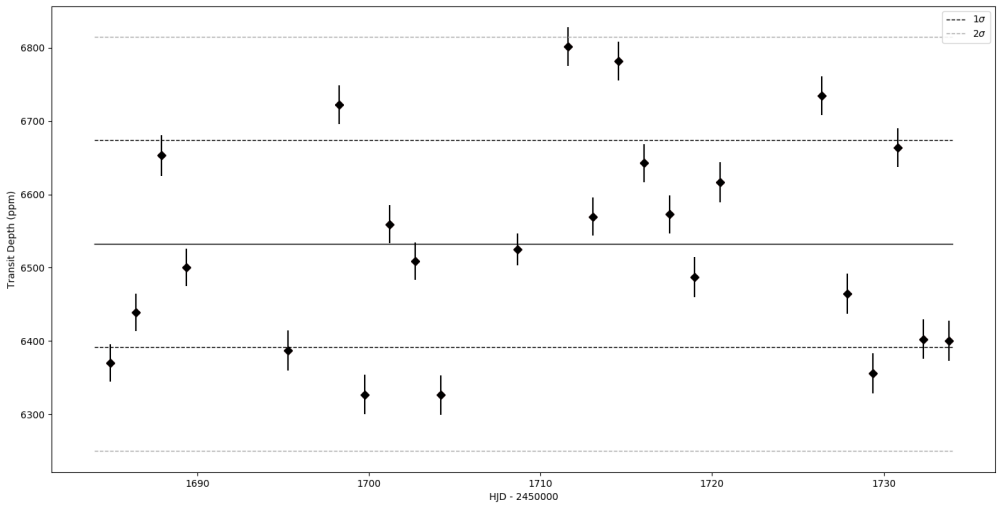

Figure 14: Transit Depth and timing for Kelt-9b

The median secondary eclipse depth is $\delta_e = 638 \pm 140$ppm which match with the value found in literature Wong et al. (2020). They derived a secondary eclipse depth of $\delta_e = 668 \pm 15$ppm. Note that their value has been derived from a phase curve model. In addition, I have also performed another fit with a MCMC procedure compiling all eclipses at once and find a similar value of $\delta_e = 665 \pm 32$ppm.

Figure 13 displays all eclipses with time of Kelt-9b in sector 14 and 15. The black line correspond to the mean and the black dashed and grey dashed lines represent the 1 and 2σ respectively. All resultant eclipses fit within 2σ which is consistant with a possible probe of variability. Too many outliers would suggest pure deviation from systematics.

Figure 14 displays all transits with time of Kelt-9b in sector 14 and 15. The median transit depth is $\delta_t = 6533 \pm 141$ppm. Detrending coefficients were switch off for the transit analysis since the variations in the light curve that are observed in figures 31 and 32 (see Appendix) doesn't interfere with the fit. The stellar photometric variation observed in the extracted light curve is due to gravity darkening Ahlers et al. (2020). The spearman coefficient for the set of data of Kelt-9b is $r_s = 0.25$ meaning that both transit and secondary eclipse variabilities are somewhat related. The p-value is $p = 0.234$ meaning that the positive correlation is quite reliable. I had to remove one transit who had no corresponding secondary eclipse to calculate this coefficient since the number of values of each variable must be identical (23 transits and 23 secondary eclipses).

7.2 WASP-121b

WASP-121b discovered in 2015 Delrez et al. (2015) with the EULER and TRAPPIST telescopes is an UHJ with an equilibrium temperature of T_{eq} = 2359±52K transiting a bright F type star (V = 10.6). With a sky-projected spin-orbit angle of 257.8±5.3° this UHJ has the singularity to be in polar orbit Delrez et al. (2015) meaning that it is transiting its star from one pole to the other. Such geometrical disposition is not common but it has already been detected in several planetary systems.

Parameters	**Description**	**Value**	**References**
M_s	Stellar Mass	1.35 $M_\odot$±0.08	Delrez et al. (2015)
R_s	Stellar Radius	1.46 $R_\odot$±0.03	Delrez et al. (2015)
[Fe/H]	Metallicity	0.13±0.09	Delrez et al. (2015)
T_{eff}	Effective Temperature	6459K±140	Delrez et al. (2015)
RA	Right Ascension	07:10:24.055	
Dec	Declination	−39:05:50.17	
M_p	Planet Mass	1.183 M_J±0.06	Delrez et al. (2015)
R_p	Planet Radius	1.865 R_J±0.04	Delrez et al. (2015)
T_{eq}	Equilibrium Temperature	2358K±52	Delrez et al. (2015)
log g	Surface Gravity	2.9258	Delrez et al. (2015)

Table 3: WASP-121 Ephemerides, stellar and planetary parameters

WASP-121b is one of the good candidates to study planetary atmosphere with its inflated radius and its very short orbital period (see table 3 for its orbital parameters taken from EXO.MAST archive). An Inflated atmosphere lead to an easier and better chemical characterisation through transmission spectroscopy. This technique has been widely used to detect chemical compounds in the atmosphere.

System	**Description**	**Value**	**Literature**
Per	Orbital Period	1.2749248±5.6e-7	Bourrier et al. (2020)
R_p/R_s	Ratio Radii	0.1235±0.00033	Bourrier et al. (2020)
i	Inclination	89.1°±0.58	Bourrier et al. (2020)
a/R_s	Semi major axis	3.82±0.0093	Bourrier et al. (2020)
Transit			
u_1	Linear Limb Darkening	0.312	From ExoCTK
u_2	Quadratic Limb Darkening	0.213	From ExoCTK
T_0	Transit Midtime	1490.724±0.001	This work
Eclipse			
Sf	Scaling Factor	0.075±0.05	This work
T_0	Eclipse Midtime	1491.362±0.001	This work

Table 4: Starting values of the system for the fit

Evidence of atomic metals have been found in the atmosphere of WASP-121b such as Cr, Na or V Ben-Yami et al. (2020). Little evidence of molecular species such as VO or TiO have been found with the Gemini Multi-Object Spectrograph (GMOS) that could explain thermal inversions present in the atmosphere Wilson et al. (2021). Water band has also been

detected in emission Mikal-Evans et al. (2020) and confirmed via a phase curve analysis in Bourrier et al. (2020). Moreover, differences in two transmission spectra found in Wilson et al. (2021) may indicate a temporal variability in the atmosphere.

Here I present the results of the best fits of the secondary eclipses and transits of WASP-121b. Table 4 lists all the parameters needed for the fit of each individual eclipse and transit. The extracted light curve is displayed in figure 35. A total of 8 eclipses and 17 transits have been analysed both with an MCMC and a Steppar procedure. I choose to show the results of the Steppar procedure.

The results are listed in table 11 & 12 along with their uncertainties and the time. The difference between the number of eclipses and transits lies in the lack of apparent eclipses in the light curve of WASP-121b. Half of them does not appear or are lost within the noise and cannot be analysed even with a detrending procedure.

Figure 15 displays all eclipses (8 in total) fitted for WASP-121b in sector 7. All eclipses depth are within 2σ except for one outlier. The median secondary eclipse depth is $\delta_e = 1280 \pm 271$ppm which is similar to the value found in literature $\delta_e = 1150 \pm 21$ppm Mikal-Evans et al. (2020). However, in a more recent paper they found a value of $\delta_e 0.482 \pm 0.039$ppt with a phase curve model Daylan et al. (2021).

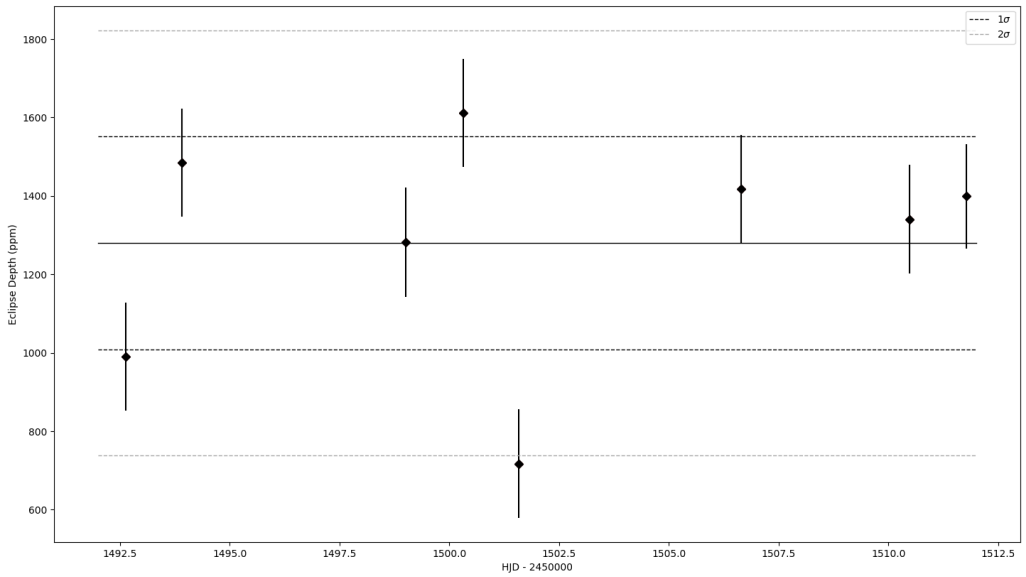

Figure 15: Secondary Eclipse Depth and timing for WASP-121b

Figure 16 displays all transits (17 in total) fitted for WASP-121b in sector 7. All transits are within 2σ except also for one outlier. The median transit depth is $\delta_t = 15355 \pm 279$ppm.

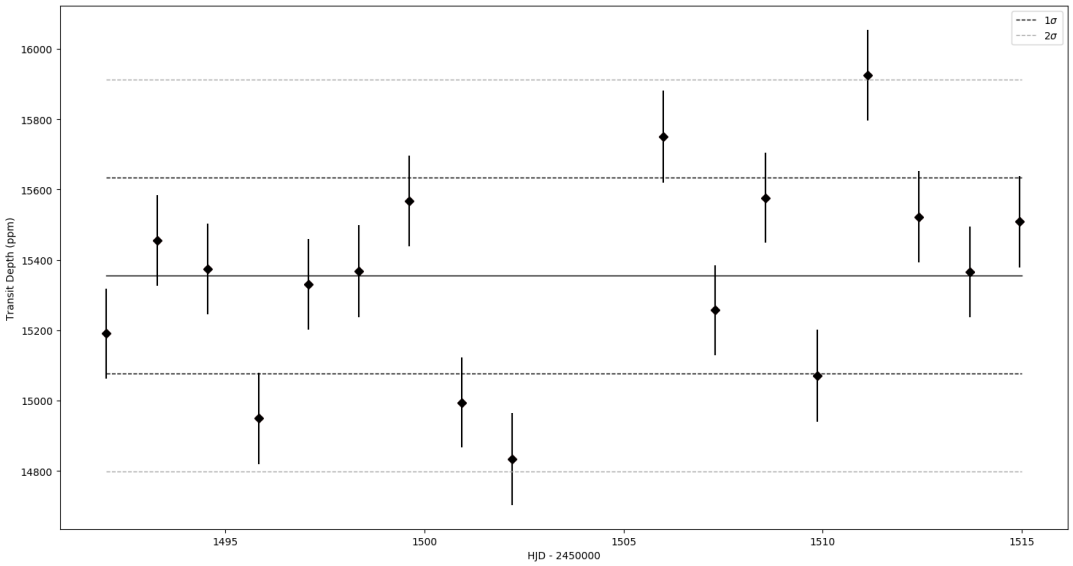

Figure 16: Transit Depth and timing for WASP-121b

The spearman coefficient for this set of data is r_s = -0.14 meaning that transit and eclipse variabilities are somewhat anti-correlated. I have found a p-values = 0.73. Only 8 out of 17 transits have been used to calculated the spearman coefficient.

WASP-121b has been observed a second time in sectors 33 and 34 of the 3rd cycle of TESS. Unfortunately, only 2 eclipses were visible in the new sectors. This very small amount of new secondary eclipses available would make a weather variability too difficult to detect.

7.3 KELT-1b

KELT-1b is a very massive object discovered in 2012 Siverd et al. (2012) with a mass of almost $30M_J$. Within this mass range these objects are called brown dwarves and are no longer considered as planets due to the fusion of deuterium in their cores. KELT-1b is orbiting a F5V star (V=10.6) with an orbital period of less than 2 days.

Here I present the results of the best fits of the secondary eclipses and transits of KELT-1b in sector 17. Table 5 lists all the stellar and planetary parameters of Kelt1 and its planetary companion taken from EXO-MAST archive. Table 6 lists all the parameters needed for the fit of each individual eclipses and transits. A total of 15 eclipses and 14 transits have been analysed both with an MCMC and a Steppar procedure. I choose to show the results from the MCMC procedure.

Parameters	**Description**	**Value**	**References**
M_s	Stellar Mass	1.335 $M_\odot$±0.063	Beatty et al. (2014)
R_s	Stellar Radius	1.471 $R_\odot$±0.045	Beatty et al. (2014)
[Fe/H]	Metallicity	0.052±0.079	Beatty et al. (2014)
T_{eff}	Effective Temperature	6516K±49	Beatty et al. (2014)
RA	Right Ascension	00:01:26.904	
Dec	Declination	+39:23:01.66	
M_p	Planet Mass	27.23 M_J±0.5	Siverd et al. (2012)
R_p	Planet Radius	1.11R_J±0.03	Siverd et al. (2012)
T_{eq}	Equilibrium Temperature	2418.4K	Beatty et al. (2014)
log g	Surface Gravity	4.7386	Siverd et al. (2012)

Table 5: Kelt1 Ephemerides, stellar and planetary parameters

System	**Description**	**Value**	**Literature**
Per	Orbital Period	1.2174928±6e-7	Beatty et al. (2020)
R_p/R_s	Ratio Radii	0.0771±0.0003	Beatty et al. (2020)
i	Inclination	87.2°±1.6	von Essen et al. (2021)
a/R_s	Semi major axis	3.63±0.051	von Essen et al. (2021)
Transit			
u_1	Linear Limb Darkening	0.319	von Essen et al. (2021)
u_2	Quadratic Limb Darkening	0.227	von Essen et al. (2021)
T_0	Transit Midtime	1764.313±0.001	This work
Eclipse			
Sf	Scaling Factor	0.075±0.05	This work
T_0	Eclipse Midtime	1764.922±0.001	This work

Table 6: Starting values of the system for the fit

The results are listed in table 13 & 14 along with their uncertainties and the time. The extracted lightcurve can be found in figure 36. Figure 17 displays all eclipses fitted for KELT-1b in sector 17. All eclipses depth fit within 2σ. The median secondary eclipse depth is $\delta_e = 365\pm67$ppm which is similar to the value found in literature $\delta_e = 371\pm47$ppm Beatty et al. (2020) or $\delta_e = 304\pm75$ppm von Essen et al. (2021) in TESS bandpass.

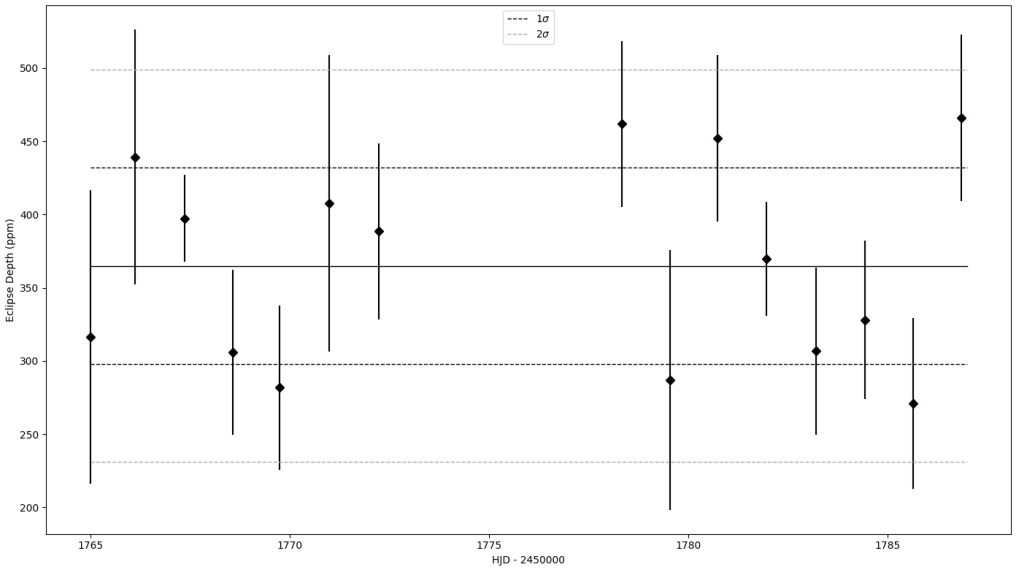

Figure 17: Secondary Eclipse Depth and timing for KELT-1b

Figure 18 displays all transits fitted for KELT-1b in sector 17. All transit depths also fit within 2σ. The median transit depth is $\delta_t = 6120 \pm 211$ppm.

The spearman coefficient for this set of data is $r_s = -0.53$ meaning that transit and eclipse variabilities are strongly anti-correlated. 1 eclipse value has been taken out to calculate the spearman coefficient. The p-value calculated out of 14 values is p-value = 0.82.

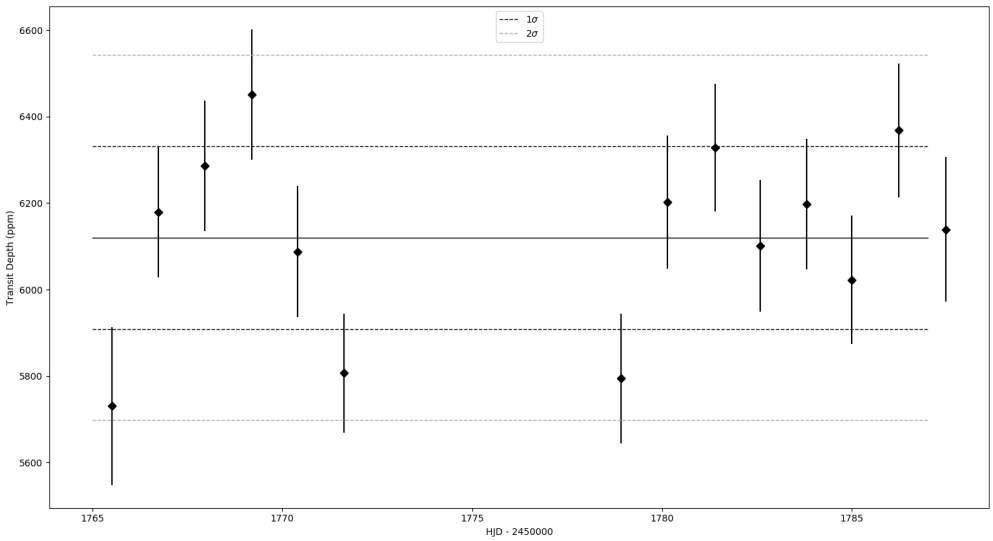

Figure 18: Transit Depth and timing for KELT-1b

7.4 WASP-18b

WASP-18b belongs to a class of UHJ with an extremely short orbital period (USP). This very massive gaseous planet has a mass of more than $10M_J$ which place it close to the limit with the brown dwarves. It is orbiting a F6 type star in less than a day implying extreme tidal interactions and irradiation on its day side. Table 7 lists all the stellar and planetary parameters of WASP18 and its planetary companion taken from EXO-MAST archive. Only four other UHJs possess an orbital period shorter than WASP-18b. Discovered in 2009 Hellier et al. (2009), this UHJ is one of the most studied exoplanet and numerous attempts have been made to characterise its atmosphere.

It has a dayside temperature of $T_d = 2894 \pm 30$K and nightside temperature of $T_n = 1430$K Arcangeli et al. (2019). Such high temperature gradient between both hemispheres is common in UHJ.

A super solar metallicity (300x) has been found Sheppard et al. (2017) with a high C/O ratio in the atmosphere. As we mentioned before, determining the metal abundances is a good proxy to figure out the type of clouds on UHJ. Moreover, no evidence of TiO or VO molecules have been yet discovered which usually explain a T/P inversion profile in a UHJ atmosphere (in WASP-121b or WASP-33b). Indeed, strong absorptions of metals like Fe or molecules like SiO can also create such inversion.

The TESS full orbital phase curve of WASP-18b revealed a lack of phase shift and a non efficient energy redistribution Shporer et al. (2019). Similar features are expected for UHJ except for the case of KELT-9b.

After an extensive analysis of this particular planetary system, I present the results of the best fits of the secondary eclipses and transits of WASP-18b. Table 8 lists all the parameters needed for the fit of each individual eclipse and transit. The extracted light curve are displayed from figure 38 to 41. Because WASP-18b has been observed multiple times in different cycles and sectors, a broad number of secondary eclipses and transits are available. Indeed, a total of 86 eclipses and 95 transits have been analysed both with

an MCMC and a Steppar procedure. I choose to only show the results from the Steppar analysis.

”

Parameters	**Description**	**Value**	**References**
M_s	Stellar Mass	1.46 $M_\odot$±0.29	Gaudi et al. (2017)
R_s	Stellar Radius	1.26 $R_\odot$±0.04	Gaudi et al. (2017)
[Fe/H]	Metallicity	0.11±0.08	Torres et al. (2012)
T_{eff}	Effective Temperature	6431±48K	Gaudi et al. (2017)
RA	Right Ascension	01:37:25.071	
Dec	Declination	−45:40:40.06	
M_p	Planet Mass	10.42 M_J±1.51	Pearson (2019)
R_p	Planet Radius	1.191R_J±0.04	Shporer et al. (2019)
T_{eq}	Equilibrium Temperature	2069±45.0 K	Chakrabarty & Sengupta (2019)
log g	Surface Gravity	3.45±0.013	Chakrabarty & Sengupta (2019)

Table 7: WASP18 Ephemerides, stellar and planetary parameters

WASP-18b display the largest sample of secondary eclipses ever in the field of exoplanet. The larger the sample of eclipses available the easier the detection of a weather variability will be and USP UHJ complete easily this requirement. The data quality and the relatively low signal to noise ratio for WASP-18b are remarquable (see light curves from figures 38 to 41). Only the sector 3 present discrepancies in some part of the light curve which may alter the fit for both transits and eclipses.

System	**Description**	**Value**	**Literature**
Per	Orbital Period	0.9414526±1e-7	Shporer et al. (2019)
R_p/R_s	Ratio Radii	0.09716±1e-5	Shporer et al. (2019)
i	Inclination	84.88°±0.33	Shporer et al. (2019)
a/R_s	Semi major axis	3.562±0.022	Shporer et al. (2019)
Transit			
u_1	Linear Limb Darkening	0.3127	Shporer et al. (2019)
u_2	Quadratic Limb Darkening	0.2192	Shporer et al. (2019)
T_0	Transit Midtime	1353.513±0.001	This work
Eclipse			
Sf	Scaling Factor	0.04±0.03	This work
T_0	Eclipse Midtime	1353.984±0.001	This work

Table 8: Starting values of the system for the fit

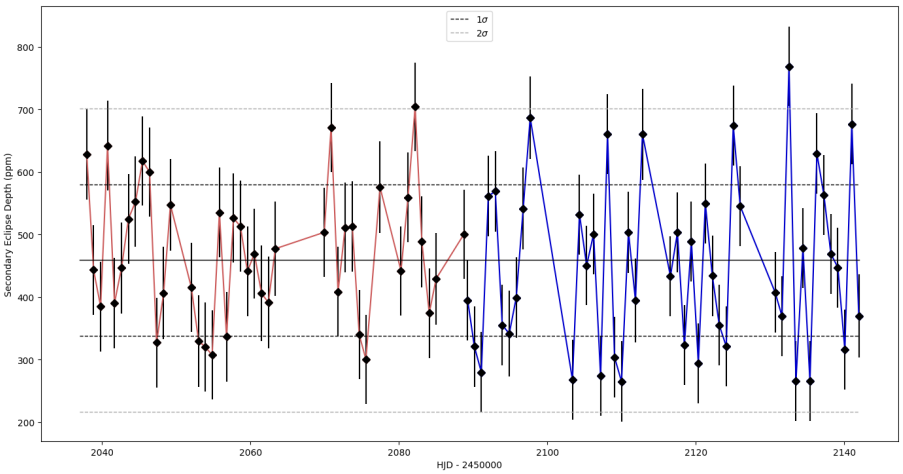

Figure 19: Secondary Eclipse Depth and timing for WASP-18b

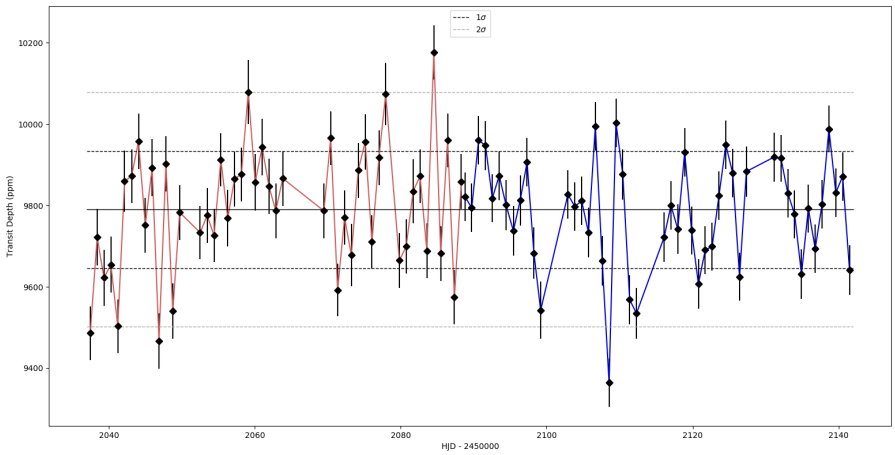

Figure 20: Transit Depth and timing for WASP-18b

Figure 19 displays all eclipses fitted for WASP-18b in all sectors. The red part correspond to the first set of data in sectors 2 and 3 from cycle 1 (41 eclipses in total) while the blue part correspond to the second set of data in sectors 29 and 30 from cycle 3 (45 eclipses in total). Because 2 years are separating cycle 1 and 3, 684 days were add to the first cycle in order to fit both sets of data within the same plot. Most eclipse depths fit within 2σ. All eclipses depths can be found in table 15 & 16 along with their uncertainties.

The median secondary eclipse depth is $\delta_e = 459 \pm 121$ppm which correspond one 1σ value close from the literature $\delta_e = 341 \pm 17$ppm Shporer et al. (2019) found from a phase curve model.

Figure 20 displays all transits (95 in total) fitted for WASP-18b in all sectors. The red part (47 transits) and blue part (48 transits) also correspond to the first and second set of observations respectively. Most transits are fitting within 2σ. We note that significant

variations can be seen either on the first cycle to another or within the same cycle. For example, a variation of more than 500ppm is found between the transit at 2108.55 days and 2110.43 days!

All results for WASP-18b transit depths are listed in table 17 & 18 along with their uncertainties and the time. The spearman rank coefficient for this system is r_s=0.07 meaning that transit and eclipse depth variabilities are not correlated. The p-value for this set of data is p-value = 0.51.

7.5 Impact of the stellar activity on the secondary eclipse depth

Photometric observations can be disturbed by several stellar-activity features such as Corona Mass Ejection (CME), flares or spots. Indeed, the presence of spots on the stellar disk during a transit event may cause a wrong determination of planetary parameters Oshagh, Santos, et al. (2013). The transit variability that we observe here may be due to stellar spots and an investigation of how they can alter or impact this variability must be done. They can be the cause of a correlation between transit and eclipse depth.

Moreover, if the exoplanet is overlapping partially or totally with a spot, one may find inconsistencies in depth, timing or duration of the transit. However, the impact of the spots on this variability depends on their sizes and their positions relative to the transiting exoplanet. An example of a spotted star with multiple spots and a transiting planet represented by a dark sphere is displayed on figure 21 below.

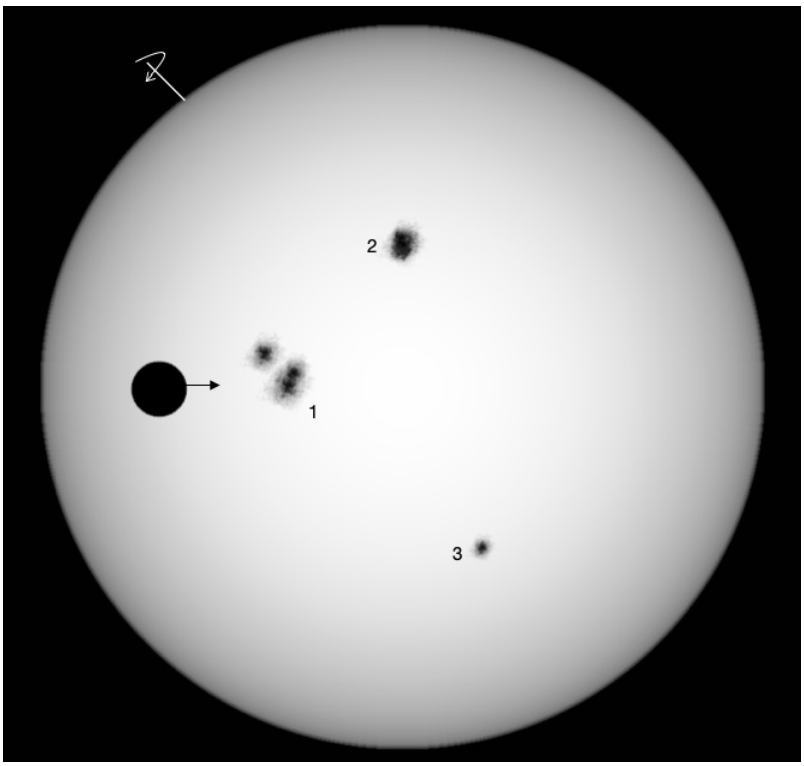

Figure 21: Spotted star with a transiting exoplanet

Stellar spots are a manifestation of the magnetic field of the star. They appear darker than the rest of the photosphere due a difference in temperature (up to 2000K cooler). During their life time on the main sequence, F and G type stars tend to spin down due to the loss of angular momentum resulting a decreasing of their activity. The lifetime of spots may vary from few days to few months for a solar type star. Since UHJ are found in general around brighter stars than HJ, the presence of spots and their influence on the light curve remain very unclear especially for UHJ orbiting F type star. A type star does not have spots.

There are several types of transit light curve anomalies that can be caused by the presence of stellar spots. The planet and the spot may overlap (configuration 1 on figure 21) resulting an irregularity on the shape of the light curve. The alteration of the incoming flux will create a dip in the curve (see figure 22). The size and the shape of the dip will mostly depend on the size of the spot and on whether if the planet is occulting partially or totally the spot during the event. A nice tool called SOAP-T can be used to simulate a transit light curve of a spotted star Oshagh, Boisse, et al. (2013). By computing the stellar, planetary and spots parameters it gives you a hint of the impact of spots on a light curve.

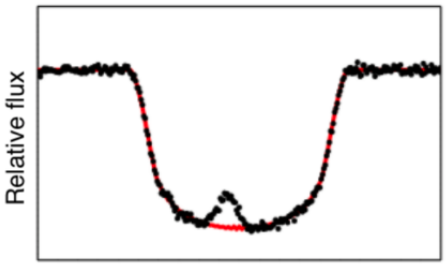

Figure 22: Spot crossing anomaly on the transit light curve

Another anomaly is due to the presence of multiple spots on the star during the transit of the planet but aren't occulted by the planet (configuration 2 and 3 on figure 21). This may not create a dip on the light curve but will on the other hand impact the overall incoming flux. Indeed, the presence of multiple spots on the stellar disk will slightly increase the transit depth and decrease the relative flux during a transit event.

However, during a secondary eclipse event a decrease of incident light from the star due the presence of spots will lead to a decrease of reflected light on the surface of the planet. The secondary eclipse depth will be then slightly smaller compare to the case of a non spotted star. Figure 24 illustrate the difference in depth between eclipses and transits for a spotted star. The black line represent the depth for a non spotted star while the dotted line shows the case with multiple spots.

Several attempts have been made to measure the impact of spots on a transit light curve of Neptune and Earth like planets transiting K and M type stars (simulating starspots in TESS transit light curves, Tregloan-Reed & Unda-Sanzana (2019)). It is possible however to estimate roughly the impact of spots on the light curve of UHJ transiting F type star using the method in Carter et al. (2011).

We want to assess how the presence of spots on the star would alter both transit and secondary eclipse depths. For the case of the secondary eclipse, only the second component of equation 2 (corresponding to the reflected part of the planet with the albedo) will be affected by the spot anomaly. The thermally emitted component is not affected. Following the method in Carter et al. (2011) the amplitude of an anomaly caused by 1 spot has the following expression :

$$\delta_s = \left(\frac{R_s}{R_*}\right)^2 (1-\alpha) \tag{15}$$

R_s being the radius of the spot, R_* is the radius of the star and $\alpha = I_s/I_*$ which correspond to the mean intensity of the spot over the intensity of the star without spot.

Equation 15 describe the simplest case where only 1 spot on the disk is present at 0° (on the equator). Let's take the case where multiple spots are present at different latitudes with different sizes. We have the new following equation:

$$\delta_s = \sum_{i=1}^{n}(\left(\frac{R_i cos\theta_i}{R_*}\right)^2 (1-\alpha_i)) \tag{16}$$

θ_i is the latitude of the spot and α_i=I_i/I_*. Using equation 16 with 1 and 2, the new expressions of the transit and eclipse depth are the following:

$$\delta_T = \left(\frac{R_p}{R_*}\right)^2 + \left(\frac{R_p}{R_*}\right)^2 \left[\sum_{i=1}^{n}\left(\frac{R_i cos\theta_i}{R_*}\right)^2 (1-\alpha_i)\right] \tag{17}$$

$$\delta_e = \left(\frac{R_p}{R_*}\right)^2 \times sf - A_g \left(\frac{R_p}{a}\right)^2 \left[\sum_{i=1}^{n}\left(\frac{R_i cos\theta_i}{R_*}\right)^2 (1-\alpha_i)\right] \tag{18}$$

R_p being the radius of the planet, sf the scaling factor, A_g the geometric albedo and a the semi major axis. Let's illustrate the influence of spots with one of our UHJ. Figure 23 displays the change in depth in ppm with increasing spot radius for WASP-18b. Blue lines correspond to the transit depth and red lines to the eclipse depth. I choose to sample 3 spots varying equally in size at different latitudes : 15° , 25°, 35° and a geometric albedo A_g = 1 (incident light is entirely reflected). In the case of the Sun, spots tend to form around latitudes of 30° to 45° at its minimum and closer to 15° when the cycle reach its maximum. Because our Sun is a main sequence G-type star, spots may occurs at different latitudes on F type stars.

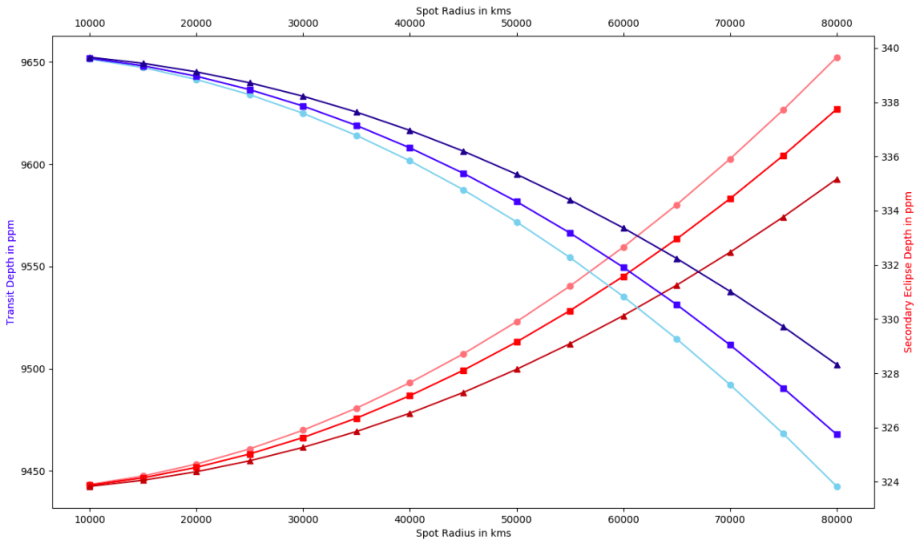

Figure 23: Impact of increasing spots size on transit and eclipse depth

We observe that for a given UHJ transiting close to equator we have a significant impact when spots have larger radius ($\sim$ 80000kms) and are close to equator (at low latitude). The upper limit for a spot was set to 80000kms which correspond roughly to the radius of

WASP-18b. For the case of 3 large spots $\sim$ 80000kms at latitude 15° (light blue and light red lines) :

An increase of 2 to 3% (up to 212 ppm) of the transit depth and a decrease of 4 to 5% (up to 16ppm) of the eclipse depth are expected.

For the case of 3 large spots $\sim$ 80000kms at latitude 35° (dark blue and dark red lines) :

An increase of 1 to 2% (up to 150ppm) of the transit depth and a decrease of 3 to 4% (up to 11ppm) of the eclipse depth are expected.

All values can be found in the Appendix in section spots (tables 19 to 21)

We may observe also that the impact on the depth for smaller spots ($\sim$ 10000kms) present at higher latitude (θ>20°) is negligible.

In summary, we notice that only very large spots close to the transit event location will have a significant impact. Furthermore, the impact value for the eclipse depth is 3 to 4 times smaller than uncertainties found in WASP-18b, WASP-121b and KELT-1b. Only KELT-9b have uncertainties 2 times larger than the impact value of spots. If the variability in depth from one orbit to another is much larger than the impact value, it is very unlikely that it is caused by the only presence of spots. The variability found in eclipse would might be then caused by the clouds in the atmosphere of the UHJ or by systematic effects.

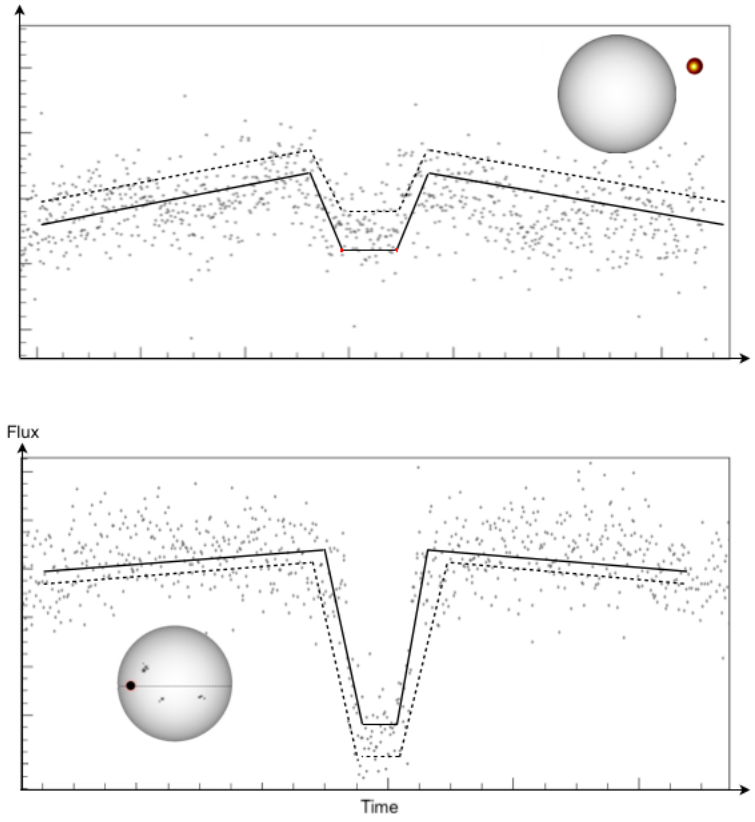

Figure 24: Impact of stellar spots on transit and eclipse depths

8 Discussion

The detection of weather variability via secondary eclipses is very challenging. Indeed, the probe of atmospheric variability in UHJ is presently limited to very few targets and submit to current limitation from astronomical instruments. Generally, most analysis lack of evidence of variability greater than the precisions of the observations or a significant impact of systematic effects on the measurements Kilpatrick et al. (2020). We noticed that, the transit depth varied more than we expected which can be due to systematics or due the presence of spots on the star. Let's evaluate the degree of variability in transit and secondary eclipse depth for each individual system.

8.1 KELT-9b

For KELT-9b, the large level of scatter found in the eclipse depths is similar that the one found in the transit depths (figure 13 and 14) meaning that no noticeable variability has been found that can only be explain by a cloud coverage. Only a significant scatter in the data points of the eclipses and a low scatter in the data points of the transits would suggest an albedo variability. Moreover, the curious and large scatter in the transits cannot be explained by spots or flares since this is a A-type exoplanetary system.

The uncertainties found for the secondary eclipse depths are rather low compare to the other analysed planetary systems since we have a good ratio of eclipse depth compare to the uncertainty of single TESS data point. In term of data quality and acquisition, eclipses of KELT-9b are the most prominent ever found in a light curve and were the easiest to fit. Indeed, KELT-9b being the hottest exoplanet, this would explain why the dip in brightness is very noticeable on the light curve.

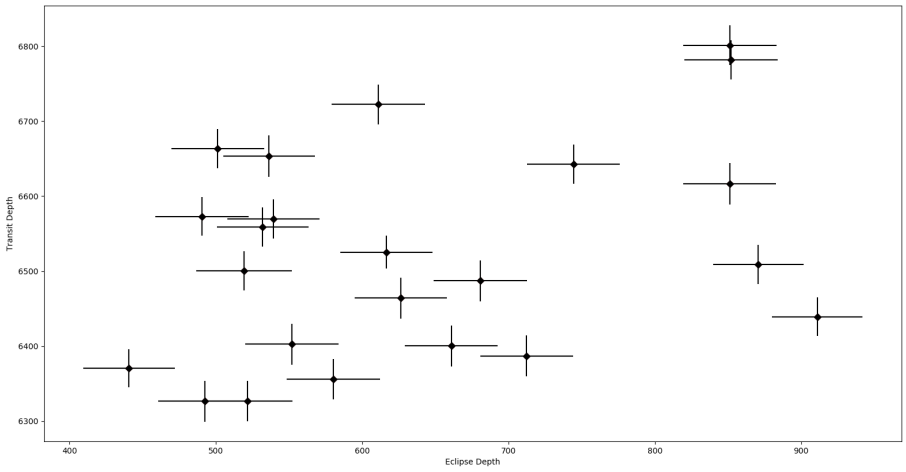

Figure 25: Correlation between eclipses and transits of KELT-9b

The complexity of this system, between the spectral type of KELT-9 and the equilibrium temperature of its planetary companion, make us redesign and reshape models in atmospheric dynamics. The formation of clouds or even their presence that originated from the nightside on the dayside of KELT9b is very improbable. If reflected clouds would be

present on KELT-9b I would expect minor fluctuations in the eclipse depth from one orbit to another of smaller than 100ppm which is not the case here. Indeed, some variations even exceeds 400ppm within one orbital period probably due to systematic effects.

Figure 25 displays the correlation between the transit and eclipse depths. I have found spearman coefficient of 0.25 with a p-values of 0.23 meaning that they they are both somewhat positively correlated with a quite reliable confidence correlation (low p). I choose arbitrary to pair as the following : eclipse + a following transit to calculate the spearman coefficient and the p-value. I had to investigate also the opposite configuration : transit + a following eclipse and the correlation did not change.

8.2 WASP-121b

WASP-121b possesses the deepest eclipse and transit depth amongst the planetary systems I have analysed due to the large planetary/star radii ($R_p/R_s > 0.1$) resulting an eclipse depth larger than 1000ppm. The distribution of the data point is uniform with the uncertainties for each individual eclipse and transit on figure 15 and 16. Excluding the value of the 5th eclipse which seems to be an outlier, most eclipses have reasonable depths. WASP-121b being much cooler than KELT-9b (1500K cooler), a variation of 200 or 300 ppm due to the presence of clouds is credible. The first analysis of the transit was done with the limb darkening coefficients found in Bourrier et al. (2020) while the second analysis was done with more accurate coefficient calculated on ExoCTK.

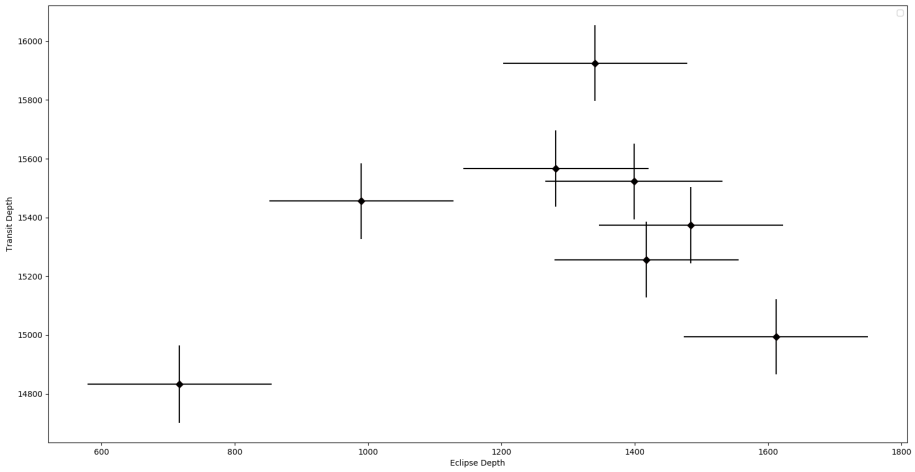

Figure 26: Correlation between eclipses and transits of WASP-121b

The lack of eclipses compare to transits analysed (almost twice as less) make the conjecture of a weather variability (periodic or not) quite difficult. As I mentioned it previously, at least the inquiry of 10 to 15 eclipses is needed. Unfortunately, the second observation in cycle 3 did not show sufficient eclipses in the light curve which could have added up to the first set of observations. The level of scatter in the transits is less pronounced compare to KELT-9b transits but still remain comparable to the one in the eclipses and can be attributed by systematics (for the higher scatter) or spots (for the lower scatter).

Figure 26 display the correlation between transits and eclipses. With a spearman coefficient of -0.14 and a p-value of 0.73, it implies that both variables are somewhat anti correlated but this correlation is very uncertain (high p-value) due the low number of pairs analysed (8 pairs). I have chosen also arbitrary to pair them as the following : eclipse + following transit. The other configuration did not change the correlation whatsoever.

8.3 KELT-1b

The stellar properties of KELT-1 are very similar to those from WASP-121 (analogous radii, masses and effective temperatures). Their companion even display a similar equilibrium temperature $\sim$ 2400K. I would expect the same level of scattering for both systems in the eclipse depth.

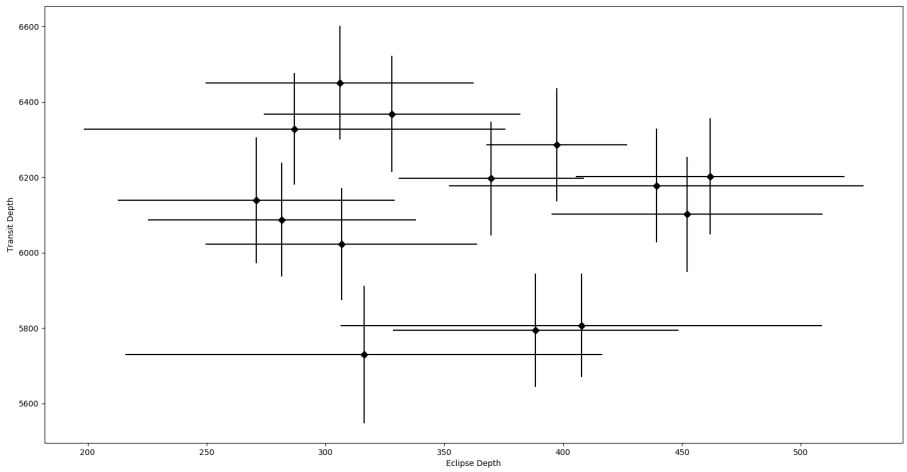

Figure 27: Correlation between eclipses and transits of KELT-1b

Such as WASP-121b, the distribution of the data points in KELT-1b is quite uniform with the uncertainties for each individual eclipses and transits (see figure 17 and 15). However, the difference between the largest and smallest eclipse depth does not exceed 200 ppm compare to the 900ppm difference that can be found in WASP-121b. The limited variation found in KELT-1b eclipse depths in my analysis may be symptomatic of weather fluctuation. This may emphasise the significant geometric albedo ($A_g \sim 0.5$) found in Beatty et al. (2020) explained by overflowing silicate or titanium night clouds onto the dayside. Figure 27 display the correlation between eclipses and transits. You may notice that no correlation has been found and data points are scatter uniformly matching a no correlation spearman coefficient of -0.06. For this case, a very high p-value of 0.82 calculated out of 14 values does not tell us anything since in the reliability of the correlation since there is no correlation between both variables. I've also chosen to pair them up in the same configuration as KELT-9b and WASP-121b.

8.4 WASP-18b

WASP-18 is sharing also similar properties with WASP-121 and KELT-1. The planetary companion, an UHJ of $\sim$10M_J possesses the largest sample of secondary eclipses available

bringing the detection of weather variability forward. Indeed, the more an object is observed, the easier is to derive its parameters, to characterise its atmosphere and to detect clouds. WASP-18b exhibit a very large baseline of observations (2 years) leading to 86 eclipses I was able to analyse.

The distribution of the data point is uniform with the uncertainties for each individual eclipses on figure 19. However the distribution for the transits on figure 20 shows several caveats : a significant amount of outliers and too large fluctuations from one orbit to another. Some outliers can be easily explained by the discrepancies present in the light curve (especially on the sector 3) but some others (in sector 29) cannot. Moreover, a drawing periodicity with a period of $\sim$7 days in the secondary eclipse depth seems to appear in the second set of data (sectors 29 and 30). Nonetheless, at this stage, no periodic signals in secondary eclipse depth have been found yet. A periodic change in the eclipse depth could be the results of a giant storm in the atmosphere of the planet.

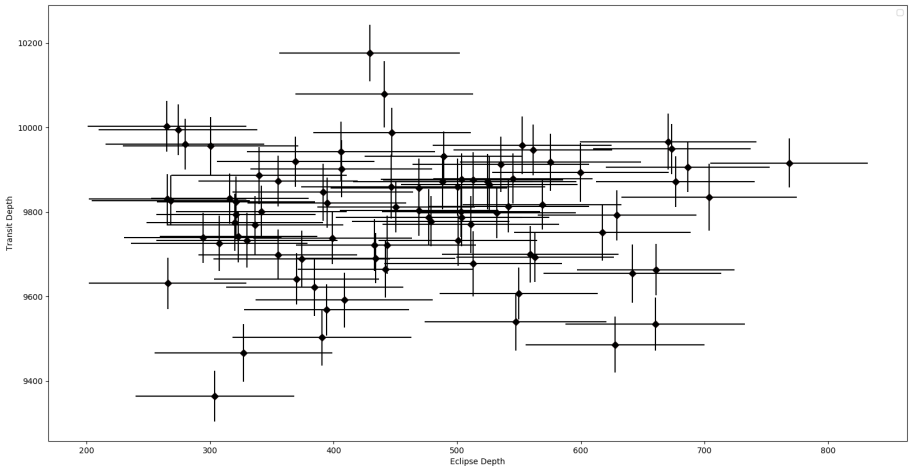

Figure 28: Correlation between eclipses and transits of WASP-18b

Figure 28 display the correlation between eclipses and transits of WASP-18. You may observe also no correlation in the distribution of points between both variables matching a spearman coefficient of 0.07. The p-value of 0.51 means that there is 50% chance that the results of the data happened by chance. I've chosen to pair them up in an opposite configuration compares to other systems : transit + following eclipse. I have also investigated the opposite configuration (eclipse + following transit) and the no-correlation remain the same. Sadly, because of the relatively high level of scatter of the transits, the variability detected in the eclipses might be caused by other effects.

8.5 Other causes of variability

If the variability in the secondary eclipse depth isn't caused by the presence of clouds in the atmosphere, it may be caused by other effects. UHJ are subject to extreme irradiation generating strong planetary winds and intensive atmospheric escape. The material expelled through space around the planet due to stellar winds will create a cometary-like tail. This planetary tail may increase the amount of reflected stellar light leading to an increase of the secondary eclipse depth. On the other hand, this cometary-tail may also impact the transit depth causing a wrong determination of the planet radius. However, the shape of the light-curve of KIC 12557548b suggesting an extrasolar planet with a comet-like tail Budaj (2013) has not been found in any of the UHJ I analysed.

The limb darkening coefficients I have used in the model to fit the transit light curve were taken from the literature. Those coefficients are very important since they play a role in the accuracy of the measurement of the planetary radius. Since the secondary eclipse depth in this work depends also on the planetary radius, inaccurate limb darkening coefficients would lead to a misestimation of the eclipse depth.

All the UHJ I have analysed except for KELT-9b are orbiting F type stars with similar properties (metallicity, surface gravity and T_{eff}). In principle, limb darkening coefficients should remain the same or be very similar. However, the coefficients they derived from a phase curve model and that I have used for WASP-121 Bourrier et al. (2020) does not match the coefficients for KELT-1 and WASP-18. I had to verify the limb darkening coefficients for the WASP-121 system via the The Exoplanet Characterization ToolKit (ExoCTK) and proceed to a second analysis of WASP-121 using the steppar command with similar limb darkening coefficients as the other systems. I noticed that the distribution of the data point didn't not change. However, each transit depths have decreased by several hundreds ppm.

Another cause that can affect the variability is the sensitivity between pixels on the CDDs that are mounted on the TESS telescope. The TPF file would be then a possible source of noise and systematics which can be seen in the resulting light curve.

Contamination from other bright objects or our moon nearby the observed star may generate a different amount of collected pixels on the CCDs causing fluctuations in the light curve. A non-detected planetary companion could also generate additional flux on the light curve.

Finally, the fitting model is based upon several parameters such as the inclination, semi major axis, the period or the mid transit time. All those parameters are essential to determine the secondary eclipse and transit depth. Since, I have let them fixed during the analysis, having them as free parameters may also impact the depth.

9 Conclusion

In this work, I studied the light curve of four exoplanetary systems and my goal was to detect variability in the secondary eclipse depth of ultra hot Jupiters in order to find out if clouds are present on their day sides. Indeed, when the planet disappear behind its host star, we called this event a secondary eclipse in the reference to the primary eclipse more commonly called a transit. Both events are the more efficient way to probe the atmosphere of an exoplanet through transmission/emission spectroscopy and photometry. In this work, only the photometric aspect has been covered on specific targets.

Ultra Hot Jupiters are definitely the best targets when it comes to the characterisation of planetary atmospheres. They are very massive and very large objects but more specifically, they undergo an intense regime of radiation heating up their atmosphere to extreme temperature. We are differentiating the class of ultra hot Jupiters from the hot Jupiters only through their equilibrium temperature. UHJ have an equilibrium temperature higher than 2000K. This exotic and unusual class of heavily irradiated planets pushes the boundaries of atmospheric characterisation. Moreover, due to their very short orbital period (few days in general), UHJ are tidally locked leading to a permanent day and night side.

This lead to very high temperature gradient between both hemispheres and complex atmospheric physical and chemical mechanisms (heat redistribution, convection, advection, thermal inversion, powerful equatorial jet, exotic chemistry and weather variability). Atmospheric dynamics of UHJ aren't totally understood yet but thanks to the tremendous amount of data collected from space surveys and ground missions, trends started to emerge. Molecules thermally dissociate on the day side and recombine on the night side Mansfield et al. (2020) leading to a cooling/heating effect that impact the overall redistribution of energy on the planet. The presence of molecules such as TiO or VO could explain the thermal inversion in the atmosphere Gandhi & Madhusudhan (2019). A damping of spectral features in the spectra and a change in the amplitude of the phase curve could be due to the presence of clouds Parmentier et al. (2021).

Nonetheless, no real detection of reflected clouds on day side of UHJ has been yet detected and remain a challenging task. The major issue being the difficulty to simply detect secondary eclipses on the first place in the light curve. However, with the ongoing space mission TESS, the task became less difficult with a significant number of observed UHJ. The selection criteria of the UHJ were mostly based on their orbital period (shorter than 3 days), equilibrium temperature (higher than 2000K) and must display a consequent number of eclipses visible on their light curve. After a careful selection of the best targets I began the analysis. The final targets selected were KELT-9b, KELT-1b, WASP-121b and WASP-18b.

KELT-9b is the hottest exoplanet ever discovered, not only it has an equilibrium temperature higher than most stars in the universe (higher than 4000K but it also orbits a B9/AO type star. Planets that form around A type star in such environment are still poorly understood but remain an excellent laboratory in planetary formation and atmospheric characterisation. KELT-9b possess the most prominent secondary eclipses in all targets observed by TESS. Despite the low uncertainties, the level of scatter found in the eclipse is similar to the one in the transit leading to no detection of weather variability.

WASP-18b is a well studied UHJ which was observed two times by TESS (with a 2 years gap) creating to the largest sample of eclipses. As i mentioned before, in order to detect weather variability on the atmosphere of a planet, a sufficient baseline of observation is required. With more than 80 eclipses analysed, WASP-18b was by far the most promising

and exciting target to work with. Unfortunately, despite this large sample of eclipse, no detection of the change of albedo was found.

WASP-121b and KELT-1b, an UHJ and a brown dwarf were also selected in the process to have higher chances of detecting clouds via multiple targets. Their analysis were also not conclusive.

All light curves were analysed with a Python script written by C. Von Essen von Essen et al. (2018) based on the Mandel-Agol Model Mandel & Agol (2002). Each eclipse depth were first inspected with an MCMC procedure (50.000 iterations with a 20% burning phase). Because of the suspiciously low uncertainties of several eclipse depth I had to proceed to a second analysis with the STEPPAR command (provided by the pyastronomy package). A detrending strategy was added in the analysis of the eclipse depths to clear out some effects in the light curve. Only the coefficients of the detrending function up to the second order were used.

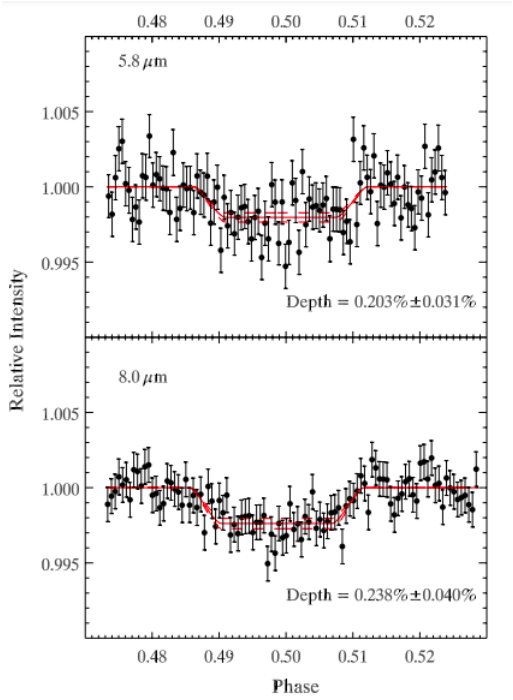

Figure 29: Binned photometry at 5.8 μm and 8 μm

After the analysis of the eclipses, I had to repeat the same procedure for the transits. Orbital and stellar parameters remained unchanged except for the scaling factor and the limb darkening coefficients. The scaling factor was taking out of the analysis and the limb darkening coefficients were activated. All transits of all targets were also analysed with an MCMC and a STEPPAR procedure.

In the attempt to detect a variability in the albedo of the planet, I had to investigate the impact of the stellar activity on both eclipse and transit depths. Indeed, stellar spots may trigger changes in the light curve either on the shape (if the planet and the spots are overlapping) or on the overall incoming stellar flux (multiple spots on the stellar disk with

no overlaping). We found that even with the presence of very large spots, the secondary eclipse is not significantly affected. However, the impact of spots is getting more important during a transit event (up to 5% change in the transit depth). It is still quite challenging to distinguish either if a variation of the depth is caused by the presence of spots or by the presence of clouds.

Furthermore, I had to investigate a possible correlation between transit depths and eclipses depths. I have used for that the spearman rank coefficient which describe statistical dependance between two variables. I had to pair each eclipse with a following transit or the other way around for all systems. WASP-18b and KELT-1b displayed no correlation meaning that there is no statistical evidence that an increase or a decrease of the transit depth would trigger the eclipse depth. On the other hand, KELT-9b showed a slightly positive correlation while WASP-121b showed a small negative correlation. However, a quite high p-value for each system except for KELT-9b suggest that the correlation isn't reliable.

No attempt or thoroughly study of eclipse variability of several exoplanets have been done in this extent. Nonetheless, I was not able to detect a change in the secondary eclipse depth higher or more prominent than the one found in the transit depth, even in the case of WASP-18b who was the most encouraging target to detect clouds. Detecting clouds on the day side of an exoplanet remain an incredible feat.

The albedo (reflected clouds) is more sensitive in the optical and the UV. Because TESS was designed to observed targets more toward the NIR, there was a significant contribution of the thermal planetary emission that trigger the analysis of the eclipse depth. However, photometry observations on the NIR have the convenience to reduce the limb darkening of the star while the disadvantage to increase it toward the UV Carter et al. (2008) which will increase the uncertainties of the planetary radius. The limb darkening does not matter in the case of the detection of clouds but photometry of secondary eclipses at different wavelengths does have an effect on the depth (see figure 29). Todorov et al. (2009)

Overall, the study of the atmosphere of UHJ has become more effective and operative in the past years and slowly extending toward smaller objects (Neptunes or Rocky planets). We have come a long way since the first detection of an exoplanet almost three decades ago. Our understanding of planetary formation and evolution is evolving every year. The characterisation of planetary atmosphere is definitely the fastest growing subfield in the exoplanet field.

10 Future work

The presence of clouds is expected on most exoplanets with an atmosphere but the peculiar case of day side of UHJ is very uncertain. Phase curve and emission spectroscopy analysis suspect their presence but no viable detection has been made yet. We expect more analysis of secondary eclipses in the future with the upcoming mission but the main challenge will be to reduce the signal to noise ratio as much as possible in order to detect more eclipses in light curves. Incorporating, the effects of the stellar activity in models would help us to have a greater view on the albedo change caused only by clouds.

The James Webb Space Telescope (JWST) and the PLAnetary Transits and Oscillations of stars (PLATO) telescope will be launched end of 2021 and 2026 respectively. The PLATO mission will have a bandpass more toward the UV (0.5–1 μm) compare to the TESS mission (0.6–1 μm) which lead to higher chances to detect reflected clouds in the optical range. The JWST is more designed largely toward the IR (0,6 à 28 μm) but will have a much greater sensitivity (10X to 100X greater than TESS) and higher angular resolution (0.07 arcsec at 2 microns) Clampin (2008).

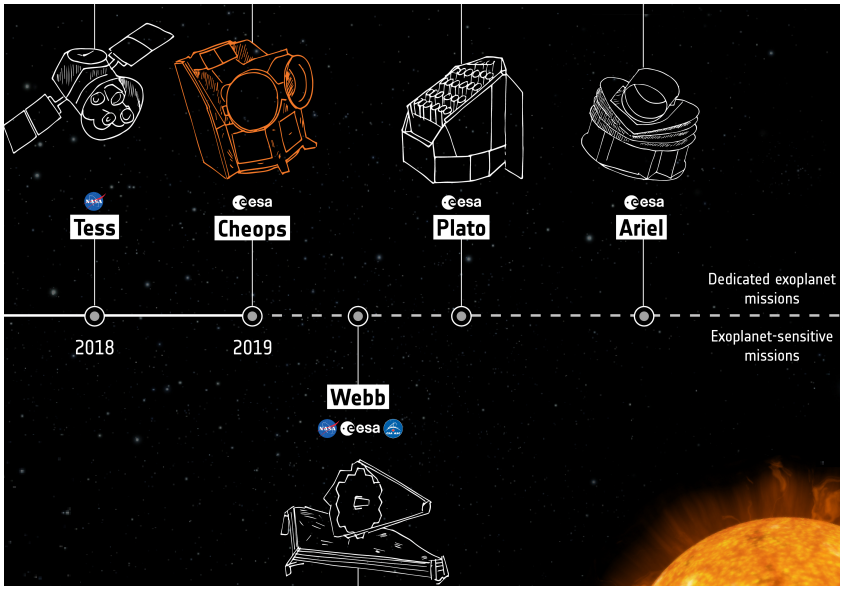

Figure 30: Correlation between eclipses and transits of KELT-1b

Finally, The European Space Agency (ESA) recently validated the space mission ARIEL (Atmospheric Remote-sensing Infrared Exoplanet Large-survey) and will launch in 2029 (at best). This mission will target pre-selected and already known exoplanets in order to characterise the chemical composition and thermal structure of their atmosphere. A very flourishing decade of promising discoveries is coming!

11 Declaration of Authorship

Declaration of originality,

I confirm that this assignment is my own work and that I have not sought or used inadmissible help of third parties to produce this work and that I have clearly referenced all sources used in the work. I have fully referenced and used inverted commas for all text directly or indirectly quoted from a source.

This work has not yet been submitted to another examination institution, neither in Germany nor outside Germany, neither in the same nor in a similar way and has not yet been published.

Potsdam,

Signed: _____

Date: _____

12 Appendix

12.1 KELT-9b

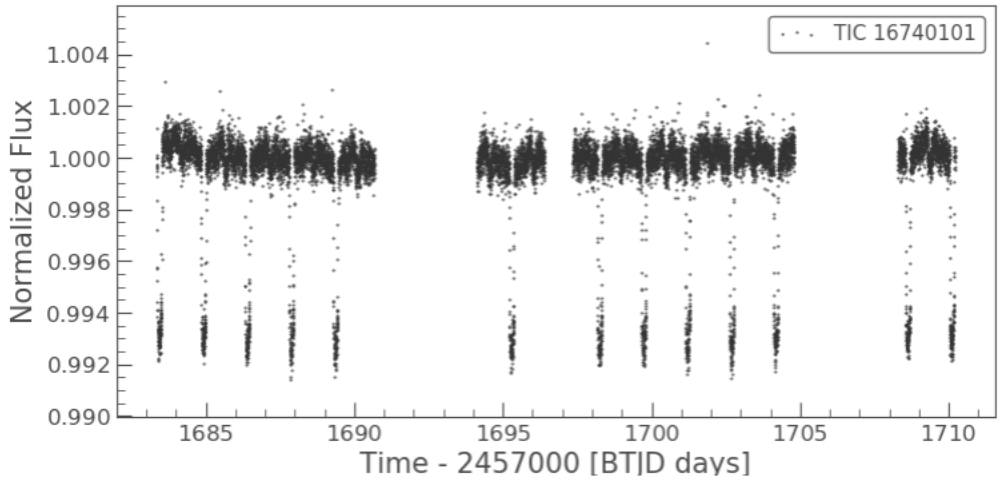

Figure 31: Light Curve extracted, Sector 14 KELT-9b

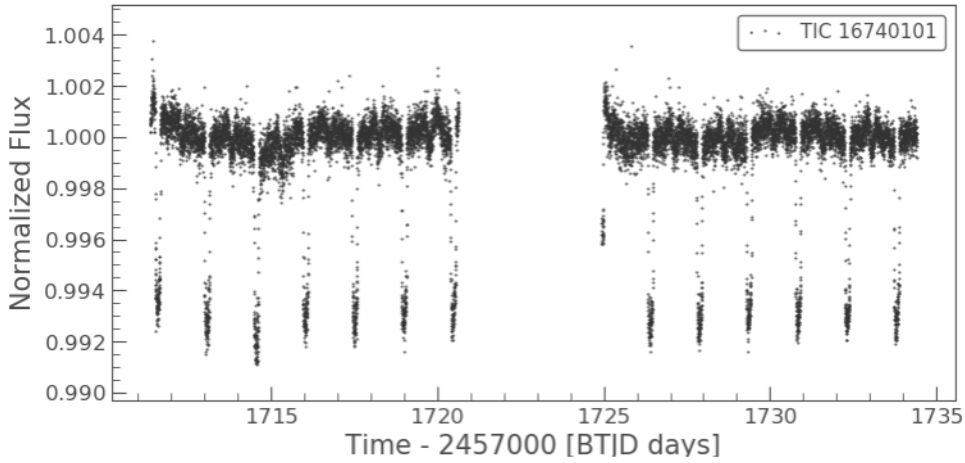

Figure 32: Light Curve extracted, Sector 15 KELT-9b

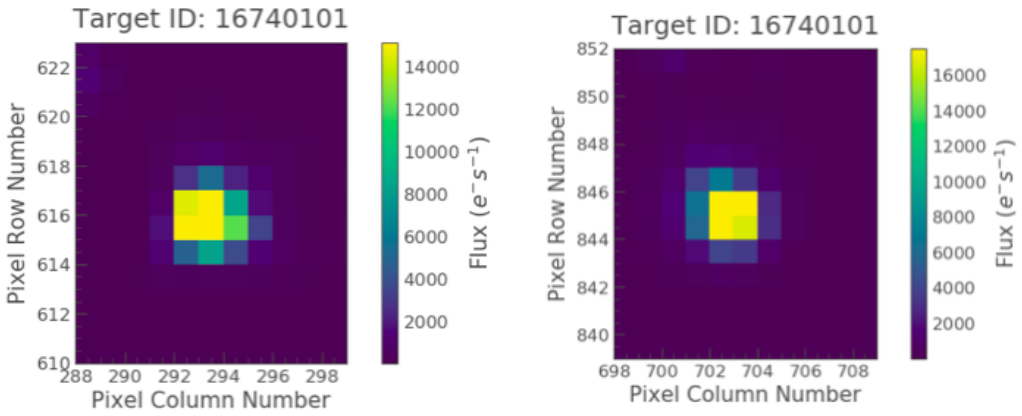

Figure 33: TPFs Sector 14 (left) and 15 (right), KELT-9b

AOR	**Sector**	**Depth(ppm)**	σ**(ppm)**
1684.19	14	440.535025101111	31.391392
1685.66	14	911.122457660167	30.942944
1687.18	14	536.305133086393	31.391392
1688.62	14	519.139204800815	32.736736
1690.11	14	712.382002620288	31.839840
1694.55	14	610.928327400018	31.839840
1696.02	14	521.494675323029	30.942944
1698.99	14	531.927652355946	31.391392
1700.49	14	870.762163944768	30.942944
1701.99	14	492.406526045601	31.839840
1703.44	14	616.536811303445	31.391392
1709.37	15	851.280179626541	31.839840
1712.28	15	539.298601966533	31.391392
1713.80	15	852.106702337171	31.839840
1715.30	15	744.391184229927	31.839840
1716.75	15	490.487074393462	31.839840
1718.23	15	680.842894898477	31.839840
1719.75	15	851.141712434387	31.839840
1727.13	15	626.329250639868	31.391392
1728.63	15	580.169666019502	31.839840
1730.12	15	501.206392466808	31.839840
1731.57	15	551.954587152959	31.839840
1733.06	15	660.868738402535	31.839840

Table 9: Results of best fit eclipse depth and time of KELT-9b

AOR	Sector	Depth(ppm)	σ(ppm)
1684.92	14	6370.52093372741	25.5665147926395
1686.42	14	6439.19934472623	25.7039572887089
1687.9	14	6653.12745487181	27.7604125681204
1689.37	14	6500.51120691314	25.8260395325227
1695.28	14	6387.10373182103	27.1997541924642
1698.26	14	6722.24358821714	26.262809203854
1699.75	14	6326.92058149973	27.0713046352001
1701.21	14	6559.02803515014	25.9420205725275
1702.7	14	6508.96057893144	25.8428184400754
1704.18	14	6326.51866168676	27.0704447645602
1708.64	14	6525.16561362786	21.8320044444966
1711.59	15	6801.19398186429	26.4165827599379
1713.05	15	6569.77518963758	25.9632652438537
1714.55	15	6781.62638478694	26.3785540415756
1716.04	15	6642.84814469866	26.1072554196113
1717.51	15	6573.04063163768	25.9697168348139
1718.99	15	6487.24333920748	27.4121493246658
1720.48	15	6616.65741609453	27.6842217405637
1726.4	15	6734.69603440295	26.2871228799116
1727.88	15	6464.18459163402	27.3633880491845
1729.37	15	6355.94499465747	27.1333276730379
1730.84	15	6663.64089533641	26.1480826007307
1732.31	15	6402.64103331522	27.2328172285476
1733.81	15	6400.40620829333	27.2280640421055

Table 10: Results of best fit transit depth and time of KELT-9b

12.2 WASP-121b

AOR	Sector	Depth(ppm)	σ(ppm)
1492.63	7	990.076634501714	138.206474265125
1493.91	7	1484.48048387899	138.206474265125
1499.01	7	1281.63370056556	138.89414460775
1500.31	7	1611.9179450702	138.206550588138
1501.58	7	717.371840425066	138.206550588138
1506.65	7	1417.66803771939	138.206550588138
1510.48	7	1340.52402773516	138.206474265125
1511.77	7	1399.04214568968	132.705798431238

Table 11: Results of best fit Eclipse depth and time of WASP-121b

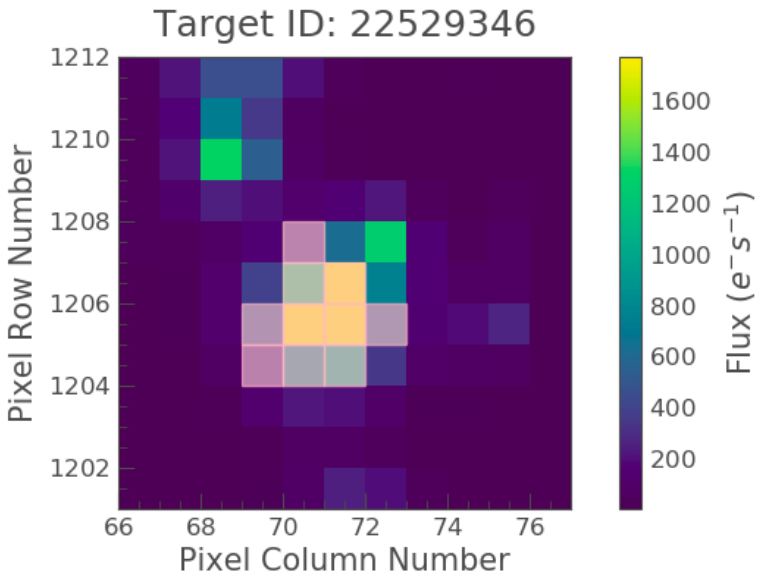

Figure 34: TPF of WASP-121b, Sector 7

AOR	**Sector**	**Depth(ppm)**	σ**(ppm)**
1492 7	7	15190.1269764468	128.30634064629
1493.28	7	15455.5169065279	129.422321015195
1494.56	7	15373.5864141918	129.078827992015
1495.84	7	14948.9162710391	129.731308184979
1497.09	7	15329.8675095956	128.895162238775
1498.34	7	15368.008431693	131.537243888916
1499.61	7	15567.4558846467	129.891403763321
1500.93	7	14994.2395153817	127.476355519468
1502.2	7	14833.3625881794	131.6672119122
1506	7	15750.677431313	130.653547806173
1507.29	7	15256.528109841	128.586469842951
1508.57	7	15576.6088298552	127.430961395883
1509.86	7	15070.5558464474	130.258051710607
1511.12	7	15925.2226740252	128.847799523302
1512.42	7	15522.4254334409	129.703405658564
1513.69	7	15365.8435441994	129.046318776855
1514.95	7	15508.6073544233	129.645661752507

Table 12: Results of best fit Transit depth and time of WASP-121b

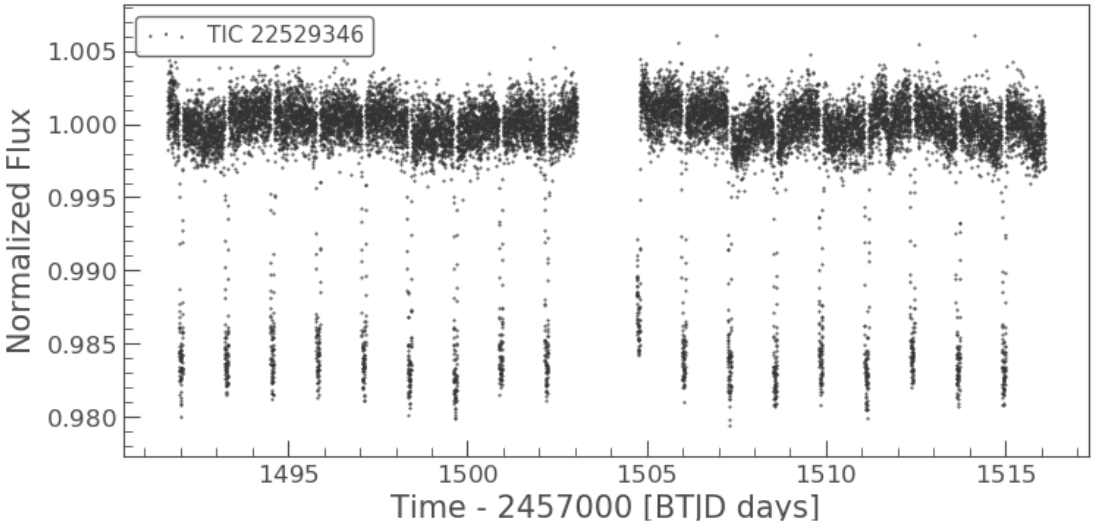

Figure 35: Light Curve of WASP-121b, Sector 7

12.3 KELT-1b

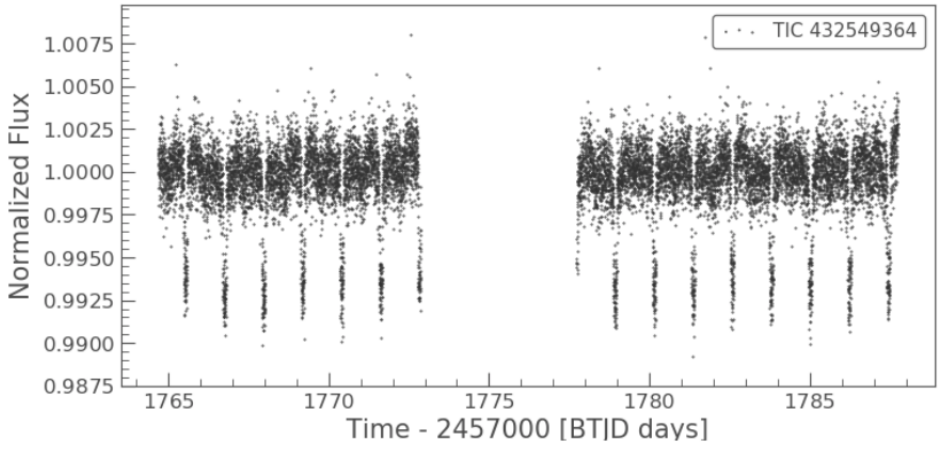

Figure 36: Light Curve of KELT-1b, Sector 17

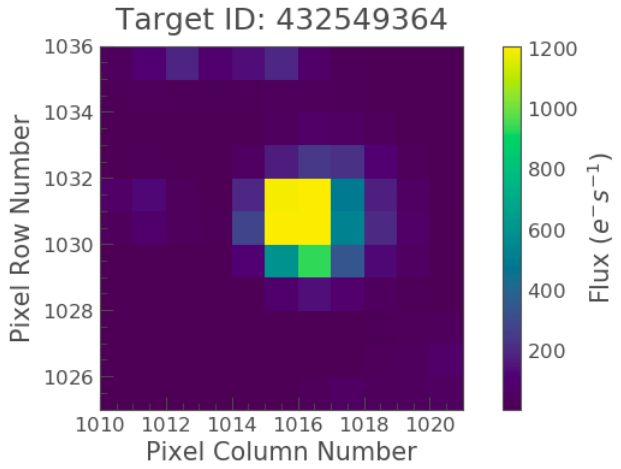

Figure 37: TPF of KELT-1b, Sector 17

AOR	**Sector**	**Depth(ppm)**	σ**(ppm)**
1765.52	17	5730.43084830662	182.293359022968
1766.74	17	6178.27942705025	150.967446449126
1767.97	17	6286.11679635167	150.311354381393
1769.2	17	6451.07590381651	150.700204895987
1770.41	17	6087.73468118978	151.466004979346
1771.62	17	5806.78562236816	137.314205562901
1778.92	17	5794.30110294866	149.552582912619
1780.14	17	6202.28800658617	154.126211087752
1781.4	17	6328.09977648247	148.232495751562
1782.58	17	6101.69200463926	152.578016345898
1783.8	17	6197.29995691549	150.856909142896
1785	17	6022.24653521677	148.899310663918
1786.23	17	6368.03283078189	154.465155954214
1787.47	17	6138.82542435261	167.373786771412

Table 13: Results of best fit Transit depth and time of KELT-1b

AOR	**Sector**	**Depth(ppm)**	σ**(ppm)**
1765	17	316.24042360598	100.26191144448
1766.12	17	439.305975231949	87.2102961682593
1767.36	17	397.283850722555	29.6011415020878
1768.58	17	306.01144223181	56.3193970663679
1769.74	17	281.714564343571	56.3414213807253
1771	17	407.751102049731	101.292116613647
1772.24	17	388.484052781349	60.0283145458721
1778.33	17	461.843622853188	56.4835526374243
1779.54	17	286.98783554258	88.6729594311144
1780.74	17	452.153616568342	56.9682138617399
1781.96	17	369.813917272005	38.9249985053623
1783.2	17	306.781288353741	57.2005914690229
1784.43	17	328.060959803817	53.9454114672994
1785.64	17	270.886568964548	58.2807996962198
1786.85	17	465.95644674579	56.914803888606

Table 14: Results of best fit Eclipse Depth and time of KELT-1b

12.4 WASP-18b

AOR	Sector	Depth(ppm)	σ(ppm)
2037.95	2	627.749412271994	72.288765542168
2038.87	2	443.156982614267	71.863537787216
2039.82	2	384.704629219233	71.863584987544
2040.75	2	641.750280064064	71.863584987544
2041.69	2	390.574765518568	72.288812742496
2042.63	2	446.365326014507	72.71399329712
2043.56	2	524.639936013069	71.863537787216
2044.52	2	552.441737135192	72.2888127424961
2045.46	2	617.486174990913	71.438310032264
2046.41	2	599.566097764804	71.438310032264
2047.36	2	327.002475432814	71.863537787216
2048.3	2	406.210654579734	73.564448807024
2049.22	2	547.196558008408	73.564496007352
2052.03	2	415.60977545753	71.438310032264
2053.02	2	329.801088394584	73.139221052072
2053.91	2	320.229475405171	71.43816843128
2054.84	2	307.514046156005	71.438310032264
2055.82	2	535.19791950276	71.438310032264
2056.78	2	336.405027214763	71.438310032264
2057.71	2	526.135807727656	71.4383100322641
2058.65	2	512.814287488933	72.71399329712
2059.59	2	441.150980933292	71.863537787216
2060.53	2	469.131324097156	71.438357232592
2061.49	2	405.762245830819	76.115862537064
2062.41	2	391.380047474924	73.1392682524
2063.35	2	477.140216347407	75.26540702716
2069.94	3	503.412590586284	71.013082277312
2070.86	3	670.732003608264	71.438357232592
2071.8	3	408.524665534428	71.438310032264
2072.75	3	510.946416912895	71.438310032264
2073.72	3	512.805338361257	71.863537787216
2074.65	3	339.751936299417	71.013082277312
2075.55	3	300.522605454684	71.01312947764
2077.45	3	575.470947712962	73.1392682524
2080.28	3	441.780260386751	71.013082277312
2081.22	3	559.097600783467	71.438357232592
2082.18	3	703.776580025723	71.013082277312
2083.09	3	488.351068026783	72.714040497448
2084.08	3	374.252135689483	71.438357232592
2085.01	3	429.18922237721	73.139221052072
2088.75	3	500.30662968269	71.013082277312

Table 15: Results of best fit Eclipse Depth and time of KELT-1b, Sector 2 and 3

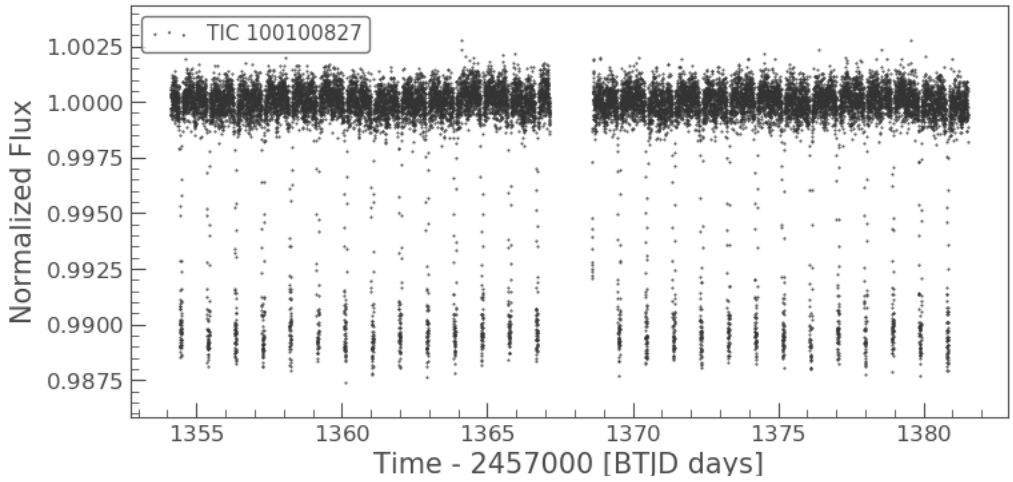

Figure 38: Light Curve of WASP-18b, Sector 2

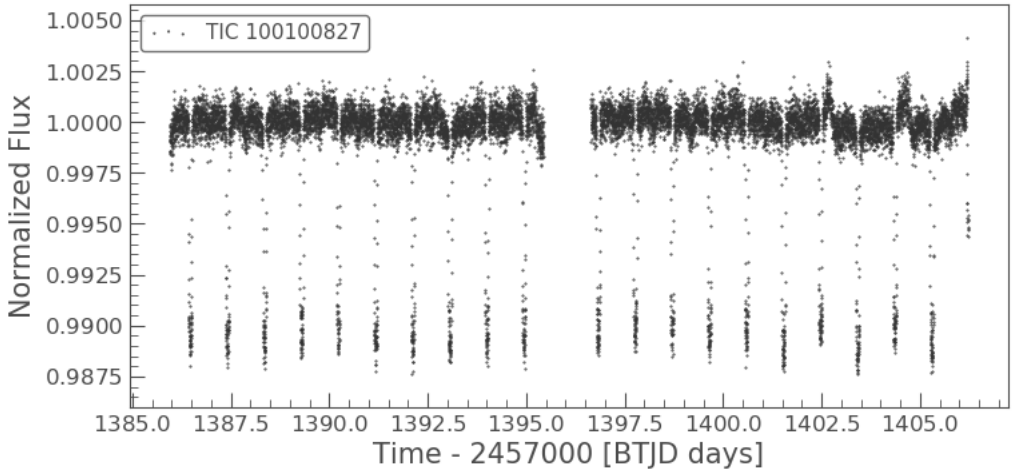

Figure 39: Light Curve of WASP-18b, Sector 3

AOR	Sector	Depth(ppm)	σ(ppm)
2089.26	29	394.676647698938	64.20943819808
2090.16	29	320.974543337454	64.20943819808
2091.1	29	279.835444922854	64.209485398408
2092.04	29	561.269918455763	64.209485398408
2092.98	29	568.837385039179	64.209485398408
2093.92	29	355.054049282838	64.20943819808
2094.86	29	341.53955037784	68.886943502552
2095.8	29	399.117008527832	64.20943819808
2096.74	29	541.468461853477	65.059893707984
2097.68	29	686.496211310693	66.33557697284
2103.37	29	268.217065909174	63.92600022844
2104.32	29	531.993355250738	63.925953028112
2105.28	29	450.426383082415	63.784257643456
2106.221	29	500.577426672917	64.20943819808
2107.16	29	274.149563581328	64.209485398408
2108.1	29	660.696911192619	63.784257643456
2109.04	29	303.79244987869	64.20943819808
2109.98	29	265.035013703305	64.20943819808
2110.92	29	503.429371467332	65.059893707984
2111.86	29	394.450151510682	66.76085192812
2112.8	29	660.177513232789	72.714040497448
2116.57	30	433.157931776978	63.784210443128
2117.51	30	503.062588243549	63.784210443128
2118.45	30	322.923528262134	63.784210443128
2119.39	30	489.048987122358	63.784210443128
2120.33	30	294.303018104656	63.784257643456
2121.27	30	549.769892178916	63.7842104431281
2122.21	30	434.075279695066	64.20943819808
2123.15	30	354.934615927627	64.20943819808
2124.09	30	320.964645026833	63.784210443128
2125.03	30	673.707732495145	63.784257643456
2125.97	30	545.09379670142	64.2094381980801
2130.67	30	407.441469314669	64.2094381980801
2131.6	30	369.281368357465	63.784257643456
2132.54	30	768.599454873819	63.784257643456
2133.48	30	265.575553827638	63.784210443128
2134.42	30	478.595969556799	63.784257643456
2135.36	30	265.835564547589	63.784210443128
2136.3	30	629.222753147272	64.20943819808
2137.24	30	563.03333209457	63.784257643456
2138.18	30	469.011379510548	63.784257643456
2139.12	30	447.119636769393	63.784210443128
2140.06	30	315.981784378323	63.784210443128
2141	30	676.538473341088	64.209485398408
2141.94	30	369.842907752747	66.76085192812

Table 16: Results of best fit Eclipse Depth and time of KELT-1b,Sector 29 and 30

AOR	**Sector**	**Depth(ppm)**	σ**(ppm)**
2037.45	2	9485.7992788754	66.2948749147226
2038.4	2	9722.20777530597	69.0899004008669
2039.32	2	9622.37563881235	68.7342615156963
2040.28	2	9654.1594355259	68.8476864549028
2041.22	2	9503.16489174484	66.3555300415737
2042.16	2	9859.85906875803	75.5410511070997
2043.11	2	9872.1093011797	65.6421792257676
2044.06	2	9957.68846339285	67.9238442684069
2044.99	2	9751.50275735012	67.2169440977765
2045.93	2	9893.20176755681	69.6948280111508
2046.87	2	9466.3294950386	68.1746514034028
2047.82	2	9902.47251068301	67.7352616767739
2048.76	2	9540.59500157625	68.4415517705833
2049.7	2	9783.08051907196	67.325688623134
2052.51	2	9733.22033739764	65.1787894971903
2053.47	2	9775.51344201899	67.2996458431856
2054.41	2	9726.00950072719	65.1546412363972
2055.35	2	9912.65026679572	65.7768247567424
2056.29	2	9768.99521464048	69.2559460067641
2057.22	2	9865.30699629568	67.6080317175059
2058.16	2	9876.45600656324	65.6566288132143
2059.11	2	10079.1785046038	78.3864955127965
2060.05	2	9856.58973656376	69.5657477397248
2061	2	9943.48569249859	69.8717215875702
2061.94	2	9847.17077068526	67.5458583573058
2062.87	2	9787.0098299543	67.3392077290414
2063.83	2	9866.59058872433	67.6124298743516
2070.4	3	9966.30957919568	65.9546165399177
2071.35	3	9591.85211672582	64.7037199998635
2072.3	3	9770.40092342463	67.2820449421595
2073.23	3	9677.68564330025	76.809411149798
2074.17	3	9886.41463986284	67.6803195708301
2075.13	3	9956.76922579371	67.9207090230731
2076.05	3	9710.64006693275	65.1031408822719
2077.01	3	9917.76445050388	67.7875417495807
2077.94	3	0074.2208941666	76.3577995185662
2079.81	3	9664.72088309678	66.9171826901254
2080.75	3	9699.57683540302	67.0377429694057
2081.7	3	9834.97652819381	79.4164972936036
2082.64	3	9872.03665440518	65.6419377018328
2083.58	3	9688.77615123899	67.0004086003041
2084.53	3	10176.1732812904	66.6454124170131
2085.48	3	9681.79545294961	66.9762675784568
2086.42	3	9960.08084321129	65.9340031876161
2087.36	3	9574.98568437353	66.6058012089686
2088.3	3	9859.0211361786	67.5864894407673

Table 17: Results of best fit Transit Depth and time of KELT-1b, Sector 2 and 3

AOR	**Sector**	**Depth(ppm)**	σ**(ppm)**
2088.79	29	9822.01182724885	59.523101752593
2089.73	29	9794.15447661724	59.4386316186793
2090.67	29	9960.37069168474	59.9408750489851
2091.61	29	9947.44768456483	59.9019775120778
2092.55	29	9817.91211111303	59.5106779592464
2093.49	29	9873.29480221329	59.6782913247404
2094.43	29	9801.13683192563	61.4418088905724
2095.43	29	9737.86729921781	61.2431743579248
2096.37	29	9812.76041370732	61.4782313120692
2097.31	29	9906.61034303271	59.7788930084738
2098.25	29	9683.13190645915	63.0408376907719
2099.17	29	9542.35035099689	70.4035004637912
2102.91	29	9827.24165859531	59.5389464879537
2103.85	29	9797.73825086218	59.4495052043064
2104.79	29	9811.14976462411	59.4901796526889
2105.73	29	9733.12389980055	61.2282565009845
2106.67	29	9994.54914429391	60.0436288490917
2107.61	29	9663.33439983436	61.0083488497164
2108.55	29	9364.64452536672	60.0580760100709
2110.43	29	9876.7444011997	61.678339678832
2111.37	29	9568.27469495319	60.7075329787853
2112.31	29	9534.50808853323	62.555168351015
2116.09	30	9721.76128367367	61.1925066046825
2117.03	30	9800.2511119662	59.4571283295698
2117.97	30	9741.62507034474	61.2549898626659
2118.91	30	9931.291615188	59.8533130803598
2119.85	30	9738.81672869184	59.2704772745054
2120.79	30	9607.15289337842	60.8307425924482
2121.73	30	9690.59335982752	59.1235513595937
2122.67	30	9698.77157163035	59.1484942570492
2123.61	30	9824.39281467777	59.5303159145998
2124.55	30	9949.03711995019	59.9067629868424
2125.49	30	9879.26299845055	59.6963257272646
2126.43	30	9624.51163289828	58.9216199797933
2127.37	30	9883.81011955611	61.7003977500463
2132.1	30	9916.04682659066	57.8137786736704
2133.04	30	9830.52154868436	59.5488813667332
2133.98	30	9778.31453119538	59.3905475466083
2134.92	30	9631.31142271595	60.9071782747316
2135.86	30	9792.55919098181	59.433790697651
2136.8	30	9693.62980476313	59.1328135038474
2137.74	30	9803.42940557211	59.4667687403013
2138.68	30	9988.23718570623	58.0238436790694
2139.62	30	9831.63906900248	59.5522659884636
2140.56	30	9871.6122327139	59.6732060339064
2141.5	30	9641.42479945401	60.9391477332893

Table 18: Results of best fit Transit Depth and time of KELT-1b,Sector 29 and 30

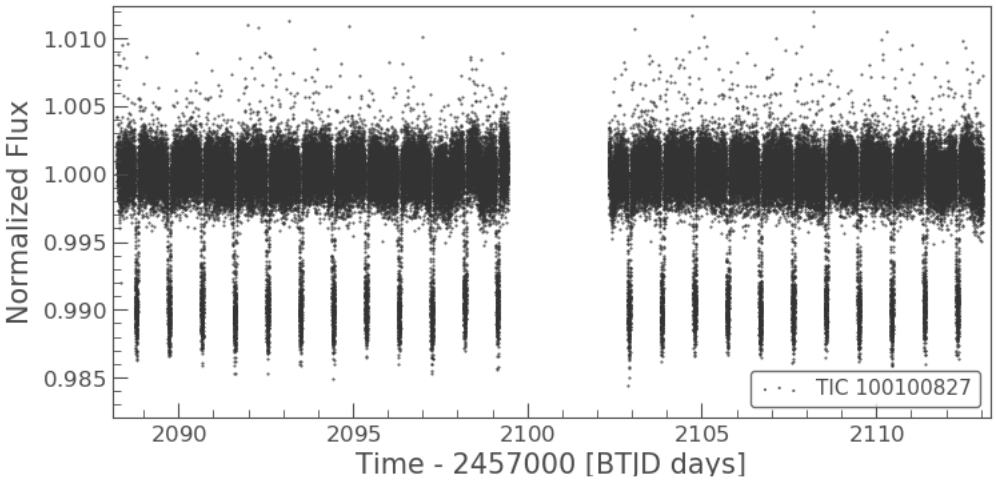

Figure 40: Light Curve of WASP-18b, Sector 29

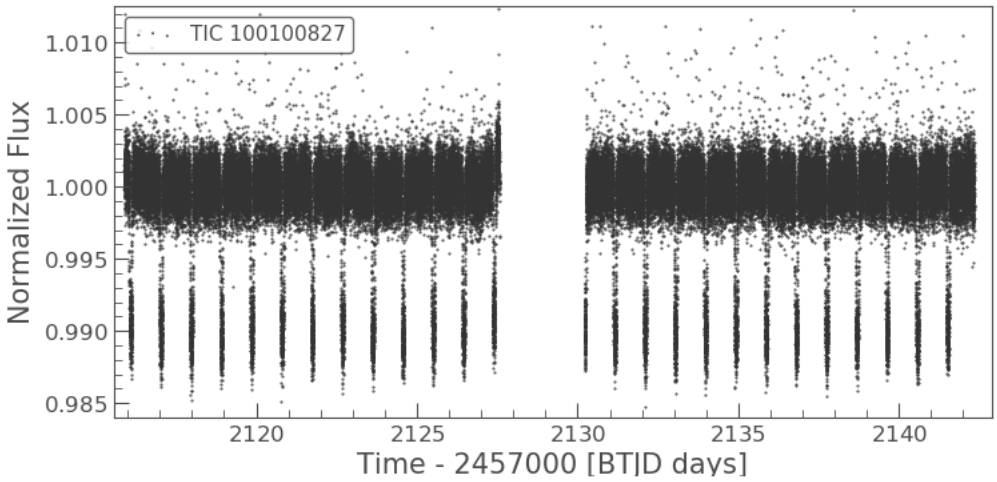

Figure 41: Light Curve of WASP-18b, Sector 30

12.5 Spots

Transit Depth	Eclipse Depth
9443.38237870516	339.592137721027
9447.5283520866	339.279357872311
9453.33271482062	338.841466084108
9460.79546690722	338.278462356419
9469.91660834639	337.590346689243
9480.69613913814	336.777119082581
9493.13405928247	335.838779536432
9507.23036877938	334.775328050796
9522.98506762886	333.586764625675
9540.39815583092	332.273089261066
9559.46963338556	330.834301956971
9580.19950029277	329.27040271339
9602.58775655256	327.581391530322
9626.63440216493	325.767268407768
9652.33943712988	323.828033345727

Table 19: Impact of stellar spots at latitude 15°

Transit Depth	Eclipse Depth
9442.98558327025	339.622072697614
9446.63556235805	339.346711569631
9451.74553308098	338.961205990455
9458.31549543902	338.465555960086
9466.34544943219	337.859761478524
9475.83539506048	337.143822545768
9486.7853323239	336.31773916182
9499.19526122243	335.381511326678
9513.06518175609	334.335139040343
9528.39509392486	333.178622302815
9545.18499772876	331.911961114094
9563.43489316778	330.53515547418
9583.14478024193	329.048205383073
9604.31465895119	327.451110840772
9626.94452929558	325.743871847278

Table 20: Impact of stellar spots at latitude 25°

Transit Depth	Eclipse Depth
9442.45098222698	339.662403982466
9445.43271001069	339.437456960549
9449.6071289079	339.122531129864
9454.9742389186	338.717626490413
9461.53404004278	338.222743042195
9469.28653228044	337.637880785209
9478.2317156316	336.963039719457
9488.36959009624	336.198219844938
9499.70015567437	335.343421161651
9512.22341236599	334.398643669598
9525.93936017109	333.363887368778
9540.84799908969	332.239152259191
9556.94932912176	331.024438340836
9574.24335026733	329.719745613715
9592.73006252639	328.325074077827

Table 21: Impact of stellar spots at latitude 35°

13 References

Ahlers, J. P., Johnson, M. C., Stassun, K. G., Colón, K. D., Barnes, J. W., Stevens, D. J., ... others (2020). Kelt-9 b's asymmetric tess transit caused by rapid stellar rotation and spin–orbit misalignment. *The Astronomical Journal*, *160*(1), 4.

Alexoudi, X., Mallonn, M., Von Essen, C., Turner, J., Keles, E., Southworth, J., ... others (2018). Deciphering the atmosphere of hat-p-12b: solving discrepant results. *Astronomy & Astrophysics*, *620*, A142.

Arcangeli, J., Désert, J.-M., Parmentier, V., Stevenson, K. B., Bean, J. L., Line, M. R., ... Showman, A. P. (2019). Climate of an ultra hot jupiter-spectroscopic phase curve of wasp-18b with hst/wfc3. *Astronomy & Astrophysics*, *625*, A136.

Barclay, T., Rowe, J. F., Lissauer, J. J., Huber, D., Fressin, F., Howell, S. B., ... others (2013). A sub-mercury-sized exoplanet. *Nature*, *494*(7438), 452–454.

Beatty, T. G., Collins, K. A., Fortney, J., Knutson, H., Gaudi, B. S., Bruns, J. M., ... others (2014). *The Astrophysical Journal*, *783*(2), 112.

Beatty, T. G., Wong, I., Fetherolf, T., Line, M. R., Shporer, A., Stassun, K. G., ... others (2020). The tess phase curve of kelt-1b suggests a high dayside albedo. *The Astronomical Journal*, *160*(5), 211.

Ben-Yami, M., Madhusudhan, N., Cabot, S. H., Constantinou, S., Piette, A., Gandhi, S., & Welbanks, L. (2020). Neutral cr and v in the atmosphere of ultra-hot jupiter wasp-121 b. *The Astrophysical Journal Letters*, *897*(1), L5.

Bodenheimer, P., Lin, D., & Mardling, R. (2001). On the tidal inflation of short-period extrasolar planets. *The Astrophysical Journal*, *548*(1), 466.

Bourrier, V., Kitzmann, D., Kuntzer, T., Nascimbeni, V., Lendl, M., Lavie, B., ... others (2020). Optical phase curve of the ultra-hot jupiter wasp-121b. *Astronomy & Astrophysics*, *637*, A36.

Brooks, S., Gelman, A., Jones, G., & Meng, X.-L. (2011). *Handbook of markov chain monte carlo*. CRC press.

Budaj, J. (2013). Light-curve analysis of kic 12557548b: an extrasolar planet with a comet-like tail. *Astronomy & Astrophysics*, *557*, A72.

Cardoso, J. V. d. M., Hedges, C., Gully-Santiago, M., Saunders, N., Cody, A. M., Barclay, T., ... others (2018). Lightkurve: Kepler and tess time series analysis in python. *Astrophysics Source Code Library*, ascl–1812.

Carter, J. A., Winn, J. N., Holman, M. J., Fabrycky, D., Berta, Z. K., Burke, C. J., & Nutzman, P. (2011). The transit light curve project. xiii. sixteen transits of the super-earth gj 1214b. *The Astrophysical Journal*, *730*(2), 82.

Carter, J. A., Yee, J. C., Eastman, J., Gaudi, B. S., & Winn, J. N. (2008). Analytic approximations for transit light-curve observables, uncertainties, and covariances. *The Astrophysical Journal*, *689*(1), 499.

Chakrabarty, A., & Sengupta, S. (2019). Precise photometric transit follow-up observations of five close-in exoplanets: update on their physical properties. *The Astronomical Journal*, *158*(1), 39.

Changeat, Q., & Edwards, B. (2021). The hubble wfc3 emission spectrum of the extremely-hot jupiter, kelt-9b. *arXiv preprint arXiv:2101.00469*.

Charbonneau, D., Allen, L. E., Megeath, S. T., Torres, G., Alonso, R., Brown, T. M., ... others (2005). Detection of thermal emission from an extrasolar planet. *The Astrophysical Journal*, *626*(1), 523.

Charbonneau, D., Brown, T. M., Noyes, R. W., & Gilliland, R. L. (2002). Detection of an extrasolar planet atmosphere. *The Astrophysical Journal*, *568*(1), 377.

Clampin, M. (2008). The james webb space telescope (jwst). *Advances in space research*, *41*(12), 1983–1991.

Cowan, N. B., & Agol, E. (2011). The statistics of albedo and heat recirculation on hot exoplanets. *The Astrophysical Journal*, *729*(1), 54.

Dawson, R. I., & Johnson, J. A. (2018). Origins of hot jupiters. *Annual Review of Astronomy and Astrophysics*, *56*, 175–221.

Daylan, T., Günther, M. N., Mikal-Evans, T., Sing, D. K., Wong, I., Shporer, A., ... others (2021). Tess observations of the wasp-121 b phase curve. *The Astronomical Journal*, *161*(3), 131.

Delrez, L., Santerne, A., Almenara, J.-M., Anderson, D., Collier-Cameron, A., Díaz, R., ... others (2015). Wasp-121 b: a hot jupiter in a polar orbit and close to tidal disruption. *arXiv preprint arXiv:1506.02471*.

Gandhi, S., & Madhusudhan, N. (2019). New avenues for thermal inversions in hot jupiters. *arXiv preprint arXiv:1903.11603*.

Gao, P., Thorngren, D. P., Lee, G. K., Fortney, J. J., Morley, C. V., Wakeford, H. R., ... Zhang, X. (2020). Aerosol composition of hot giant exoplanets dominated by silicates and hydrocarbon hazes. *Nature Astronomy*, 1–6.

Gaudi, B. S., Stassun, K. G., Collins, K. A., Beatty, T. G., Zhou, G., Latham, D. W., ... others (2017). A giant planet undergoing extreme-ultraviolet irradiation by its hot massive-star host. *Nature*, *546*(7659), 514–518.

Hellier, C., Anderson, D., Cameron, A. C., Gillon, M., Hebb, L., Maxted, P., ... others (2009). An orbital period of 0.94 days for the hot-jupiter planet wasp-18b. *Nature*, *460*(7259), 1098–1100.

Keating, D., Cowan, N. B., & Dang, L. (2019). Uniformly hot nightside temperatures on short-period gas giants. *Nature Astronomy*, *3*(12), 1092–1098.

Kilpatrick, B. M., Kataria, T., Lewis, N. K., Zellem, R. T., Henry, G. W., Cowan, N. B., ... others (2020). Evaluating climate variability of the canonical hot-jupiters hd 189733b and hd 209458b through multi-epoch eclipse observations. *The Astronomical Journal*, *159*(2), 51.

Kreidberg, L., Line, M. R., Bean, J. L., Stevenson, K. B., Désert, J.-M., Madhusudhan, N., ... others (2015). A detection of water in the transmission spectrum of the hot jupiter wasp-12b and implications for its atmospheric composition. *The Astrophysical Journal*, *814*(1), 66.

Lothringer, J. D., Rustamkulov, Z., Sing, D. K., Gibson, N. P., Wilson, J., & Schlaufman, K. C. (2020). A new window into planet formation and migration: Refractory-to-volatile elemental ratios in ultra-hot jupiters. *arXiv preprint arXiv:2011.10626*.

Madhusudhan, N. (2019). Exoplanetary atmospheres: Key insights, challenges, and prospects. *Annual Review of Astronomy and Astrophysics*, *57*, 617–663.

Mallonn, M., Köhler, J., Alexoudi, X., von Essen, C., Granzer, T., Poppenhaeger, K., & Strassmeier, K. (2019). Low albedos of hot to ultra-hot jupiters in the optical to near-infrared transition regime. *Astronomy & Astrophysics*, *624*, A62.

Mallonn, M., & Strassmeier, K. G. (n.d.). Transmission spectroscopy of hat-p-32b with the lbt: confirmation of clouds/hazes in the planetary atmosphere. *Astronomy & Astrophysics*.

Mandel, K., & Agol, E. (2002). Analytic light curves for planetary transit searches. *The Astrophysical Journal Letters*, *580*(2), L171.

Mansfield, M., Bean, J. L., Stevenson, K. B., Komacek, T. D., Bell, T. J., Tan, X., ... others (2020). Evidence for h2 dissociation and recombination heat transport in the atmosphere of kelt-9b. *The Astrophysical Journal Letters*, *888*(2), L15.

Merritt, S. R., Gibson, N. P., Nugroho, S. K., de Mooij, E. J., Hooton, M. J., Matthews, S. M., ... others (2020). Non-detection of tio and vo in the atmosphere of wasp-121b using high-resolution spectroscopy. *Astronomy & Astrophysics*, *636*, A117.

Mikal-Evans, T., Sing, D. K., Kataria, T., Wakeford, H. R., Mayne, N. J., Lewis, N. K., ... Spake, J. J. (2020). Confirmation of water emission in the dayside spectrum of the ultrahot jupiter wasp-121b. *Monthly Notices of the Royal Astronomical Society*, *496*(2), 1638–1644.

Moses, J. I. (2014). Chemical kinetics on extrasolar planets. *Philosophical Transactions of the Royal Society A: Mathematical, Physical and Engineering Sciences*, *372*(2014), 20130073.

Oshagh, M., Boisse, I., Boué, G., Montalto, M., Santos, N., Bonfils, X., & Haghighipour, N. (2013). Soap-t: a tool to study the light curve and radial velocity of a system with a transiting planet and a rotating spotted star. *Astronomy & Astrophysics*, *549*, A35.

Oshagh, M., Santos, N. C., Boisse, I., Boue, G., Montalto, M., Dumusque, X., & Haghighipour, N. (2013). Effect of stellar spots on high-precision transit light-curve. *Astronomy & Astrophysics*, *556*, A19.

Parmentier, V., Showman, A. P., & Fortney, J. J. (2021). The cloudy shape of hot jupiter thermal phase curves. *Monthly Notices of the Royal Astronomical Society*, *501*(1), 78–108.

Pearson, K. A. (2019). A search for multiplanet systems with tess using a bayesian n-body retrieval and machine learning. *The Astronomical Journal*, *158*(6), 243.

Plachy, E., Molnár, L., Bódi, A., Skarka, M., Szabó, P., Szabó, R., ... Pope, B. J. (2019). Extended aperture photometry of k2 rr lyrae stars. *The Astrophysical Journal Supplement Series*, *244*(2), 32.

Ricker, G. R., Winn, J. N., Vanderspek, R., Latham, D. W., Bakos, G. Á., Bean, J. L., ... others (2014). Transiting exoplanet survey satellite. *Journal of Astronomical Telescopes, Instruments, and Systems*, *1*(1), 014003.

Santerne, A., Moutou, C., Barros, S., Damiani, C., Díaz, R., Almenara, J.-M., ... Hébrard, G. (2012). Sophie velocimetry of kepler transit candidates-vi. an additional companion in the koi-13 system. *Astronomy & Astrophysics*, *544*, L12.

Schlaufman, K. C. (2018). Evidence of an upper bound on the masses of planets and its implications for giant planet formation. *The Astrophysical Journal*, *853*(1), 37.

Seager, S., & Deming, D. (2010). Exoplanet atmospheres. *Annual Review of Astronomy and Astrophysics*, *48*, 631–672.

Sedaghati, E., Boffin, H. M., MacDonald, R. J., Gandhi, S., Madhusudhan, N., Gibson, N. P., ... Rauer, H. (2017). Detection of titanium oxide in the atmosphere of a hot jupiter. *Nature*, *549*(7671), 238–241.

Sheppard, K. B., Mandell, A. M., Tamburo, P., Gandhi, S., Pinhas, A., Madhusudhan, N., & Deming, D. (2017). Evidence for a dayside thermal inversion and high metallicity for the hot jupiter wasp-18b. *The Astrophysical Journal Letters*, *850*(2), L32.

Showman, A. P., & Guillot, T. (2002). Atmospheric circulation and tides of "51 pegasus b-like" planets. *Astronomy & Astrophysics*, *385*(1), 166–180.

Shporer, A., Wong, I., Huang, C. X., Line, M. R., Stassun, K. G., Fetherolf, T., ... others (2019). Tess full orbital phase curve of the wasp-18b system. *The Astronomical Journal*, *157*(5), 178.

Siegel, S. (1957). Nonparametric statistics. *The American Statistician*, *11*(3), 13–19.

Siverd, R. J., Beatty, T. G., Pepper, J., Eastman, J. D., Collins, K., Bieryla, A., ... others (2012). Kelt-1b: a strongly irradiated, highly inflated, short period, 27 jupiter-mass companion transiting a mid-f star. *The Astrophysical Journal*, *761*(2), 123.

Stassun, K. G., Oelkers, R. J., Pepper, J., Paegert, M., De Lee, N., Torres, G., ... others (2018). The tess input catalog and candidate target list. *The Astronomical Journal*, *156*(3), 102.

Todorov, K., Deming, D., Harrington, J., Stevenson, K. B., Bowman, W. C., Nymeyer, S., ... Bakos, G. A. (2009). Spitzer irac secondary eclipse photometry of the transiting extrasolar planet hat-p-1b. *The Astrophysical Journal*, *708*(1), 498.

Torres, G., Fischer, D. A., Sozzetti, A., Buchhave, L. A., Winn, J. N., Holman, M. J., & Carter, J. A. (2012). Improved spectroscopic parameters for transiting planet hosts. *The Astrophysical Journal*, *757*(2), 161.

Tregloan-Reed, J., & Unda-Sanzana, E. (2019). Simulations of starspot anomalies within tess exoplanetary transit light curves-i. detection limits of starspot anomalies in tess light curves. *Astronomy & Astrophysics*, *630*, A114.

Tremblin, P., Chabrier, G., Mayne, N., Amundsen, D., Baraffe, I., Debras, F., ... Fromang, S. (2017). Advection of potential temperature in the atmosphere of irradiated exoplanets: a robust mechanism to explain radius inflation. *The Astrophysical Journal*, *841*(1), 30.

Vallis, G. K. (2017). *Atmospheric and oceanic fluid dynamics*. Cambridge University Press.

von Essen, C., Mallonn, M., Piette, A., Cowan, N., Madhusudhan, N., Agol, E., ... others (2021). Tess unveils the optical phase curve of kelt-1b.

von Essen, C., Ofir, A., Dreizler, S., Agol, E., Freudenthal, J., Hernández, J., ... others (2018). Kepler object of interest network-i. first results combining ground-and space-based observations of kepler systems with transit timing variations. *Astronomy & Astrophysics*, *615*, A79.

von Essen, C., Stefansson, G., Mallonn, M., Pursimo, T., Djupvik, A., Mahadevan, S., ... Dreizler, S. (2019). First light of engineered diffusers at the nordic optical telescope reveal time variability of the optical eclipse depth of wasp-12b. *Astronomy & Astrophysics*, *628*, A115.

Wilson, J., Gibson, N. P., Lothringer, J. D., Sing, D. K., Mikal-Evans, T., de Mooij, E. J., ... Watson, C. A. (2021). Gemini/gmos optical transmission spectroscopy of wasp-121b: signs of variability in an ultra-hot jupiter? *arXiv preprint arXiv:2103.05698*.

Wong, I., Knutson, H. A., Kataria, T., Lewis, N. K., Burrows, A., Fortney, J. J., ... others (2016). 3.6 and 4.5 μm spitzer phase curves of the highly irradiated hot jupiters wasp-19b and hat-p-7b. *The Astrophysical Journal*, *823*(2), 122.

Wong, I., Shporer, A., Kitzmann, D., Morris, B. M., Heng, K., Hoeijmakers, H. J., ... others (2020). Exploring the atmospheric dynamics of the extreme ultrahot jupiter kelt-9b using tess photometry. *The Astronomical Journal*, *160*(2), 88.

Zhou, G., Bakos, G., Bayliss, D., Bento, J., Bhatti, W., Brahm, R., ... others (2019). Hats-70b: A 13 mj brown dwarf transiting an a star. *The Astronomical Journal*, *157*(1), 31.

Zhou, G., Rodriguez, J. E., Collins, K. A., Beatty, T., Oberst, T., Heintz, T. M., ... others (2016). Kelt-17b: a hot-jupiter transiting an a-star in a misaligned orbit detected with doppler tomography. *The Astronomical Journal*, *152*(5), 136.